



Akıllı Şehirlerdeki Multikopter Şarj İstasyonları için Simülasyon Tabanlı Karar Zekası Modeli

Kübra ÇELİK^{1*}, Haluk EREN²

^{1,2}Hava Trafik Kontrol Bölümü, Sivil Havacılık Yüksekokulu, Fırat Üniversitesi, Elazığ, Türkiye.

¹k.celik@firat.edu.tr, ²heren@firat.edu.tr

Geliş Tarihi: 19.8.2025
Kabul Tarihi: 06.11.2025

Düzeltilme Tarihi: 20.9.2025

doi: <https://doi.org/10.62520/fujece.1768822>
Araştırma Makalesi

Alıntı: K. Çelik ve H. Eren, "Akıllı şehirlerdeki multikopter şarj istasyonları için simülasyon tabanlı karar zekası modeli", Fırat Üni. Deny. ve Hes. Müh. Derg., vol. 5, no 1, pp. 169-217, Şubat 2026.

Öz

Kentsel hava hareketliliği giderek artan biçimde otonom çok rotorlu hava aracı filolarına dayanmaktadır. Ancak bu filoların operasyonel sürdürülebilirliği, akıllı şarj altyapılarının eksikliği nedeniyle hâlâ önemli ölçüde sınırlıdır. Bu çalışma, akıllı şehir koşulları altında altı farklı çok rotorlu şarj istasyonu arketipini değerlendirmek üzere tasarlanmış simülasyon temelli bir karar zekası modeli sunmaktadır. Önerilen çerçeve, Güvenlik, Altyapı Maliyeti, Lojistik Uyumluluk, Akıllı Şehir Entegrasyonu ve Sürdürülebilirlik olmak üzere beş normalleştirilmiş değerlendirme faktörünü, şeffaf ve denetlenebilir bir çok ölçütlü karar yapısı içinde birleştirmektedir. Analitik titizliği ve yorumlanabilirliği güvence altına almak amacıyla iki tamamlayıcı değerlendirme modu geliştirilmiştir. İlk mod olan Mode A, eşit ağırlıklar kullanan ve yönetsel açıklığı koruyan tekrarlanabilir bir temel yapı sunmaktadır. İkinci mod olan Mode B ise altyapı kapasitesi ile lojistik akış arasında kontrollü bir ilişki kuran sınırlı bir koordinasyon operatörü olarak işlev görmek ve etkileşim farkındalığını sıralama mantığını değiştirmeden sisteme dâhil etmektedir. Karar verileri Latin Hiperküp Örnekleme yöntemiyle sentetik olarak üretilmiş, belirsizlik ise bootstrap yeniden örnekleme tekniğiyle nicel biçimde hesaplanmıştır. Her iki modun da kararlılığı analitik olarak doğrulanmış, sonuçlar Kendall's τ değerinin 0.90'ın üzerinde, Top-k korunum oranının ise yüzde 95'in üzerinde olduğunu göstermiştir. Bu bulgular, etkileşim farkındalığının yorum gücünü artırırken analitik tutarlılığı koruduğunu kanıtlamaktadır. Elde edilen sonuçlar, Son Mil ve İlk Mil istasyonlarının farklı kentsel morfolojilerde en yüksek bileşik verimlilik puanlarını (sırasıyla 0.82 ve 0.80) koruduğunu ortaya koymuştur. Çatı ve Elektrikli Araç Entegreli istasyon konfigürasyonları da yenilenebilir enerjiyle uyumlu senaryolarda rekabetçi bir ölçeklenebilirlik ve gelişmiş performans sergilemiştir. Geliştirilen genel çerçeve, kentsel drone şarj ağlarının planlanması, uygulanması ve ampirik olarak kalibre edilmesi için tekrarlanabilir, politika açısından uyumlu ve bilimsel olarak izlenebilir bir temel sunmaktadır. Ayrıca veri eksikliği bulunan ortamlarda karar alma süreçlerine yönelik tutarlı bir yönetsel yol haritası oluşturmakta, analitik şeffaflık ve operasyonel anlamlılığın gelecekteki pilot uygulamalar boyunca korunmasını sağlamaktadır.

Anahtar kelimeler: Otonom İHA şarjı, Akıllı karar, Akıllı şehir lojistiği, Sürdürülebilirlik, Kentsel hava mobilitesi

*Yazılan yazar

İntihal Kontrol: Evet – Turnitin

Şikayet: fujece@firat.edu.tr

Telif Hakkı ve Lisans: Dergide yayın yapan yazarlar, CC BY-NC 4.0 kapsamında lisanslanan çalışmalarının telif hakkını saklı tutar.



Simulation Based Decision Intelligence Model for Multicopter Charging Stations in Smart Cities

Kübra CELIK^{1*}, Haluk EREN²

^{1,2}Air Traffic Control Department, Civil Aviation School, Firat University, Elazığ, Türkiye.

¹ k.celik@firat.edu.tr, ²heren@firat.edu.tr

Received: 19.8.2025
Accepted: 06.11.2025

Revision: 20.9.2025

doi: <https://doi.org/10.62520/fujece.1768822>
Research Article

Citation: K. Çelik and H. Eren "Simulation based decision intelligence model for multicopter charging stations in smart cities", *Firat Univ. Jour. of Exper. and Comp. Eng.*, vol. 5, no 1, pp. 169-217, February 2026.

Abstract

Urban air mobility increasingly relies on autonomous multicopter fleets whose operational sustainability remains constrained by the absence of intelligent recharging infrastructures. This study introduces a simulation based decision intelligence model designed to evaluate six multicopter charging station archetypes under smart city conditions. The proposed framework integrates five normalized evaluation factors, namely Security, Infrastructure Cost, Logistics Compatibility, Smart City Integration, and Sustainability, within a transparent and auditable multi-criteria decision framework. Two complementary evaluation modes are developed to ensure analytical rigor and interpretability. The first mode, Mode A, represents a reproducible baseline configuration that employs equal weighting to retained methodological clarity. The second mode, Mode B, functions as a bounded coordination operator that establishes a controlled relationship between infrastructure capacity and logistics flow, enabling interaction informed evaluation without altering the ranking logic. Synthetic decision data are generated through Latin Hypercube Sampling, while bootstrap resampling is used to quantify uncertainty. The stability of both modes is analytically verified, showing that Kendall's τ exceeds 0.90 and Top-k retention remains above 95 percent. These results demonstrate that introducing interaction awareness refines interpretability while maintaining analytical consistency across uncertainty ranges. The findings reveal that Last Mile and First Mile stations maintain the highest composite efficiency scores, 0.82 and 0.80 respectively, across various urban morphologies. Roof and Electric Vehicle Coupled configurations also display competitive scalability and improved performance when aligned with renewable energy scenarios. The overall framework provides a reproducible, policy aligned, and scientifically traceable foundation for the planning, deployment, and empirical calibration of urban drone charging networks. It further establishes a consistent methodological pathway for decision making in data scarce environments, ensuring that analytical transparency and operational relevance are sustained throughout future pilot implementations.

Keywords: Autonomous UAV recharging, Intelligent decision, Smart city logistics, Sustainability, Urban air mobility (UAM)

*Corresponding author

1. Introduction

Unmanned Aerial Vehicles (UAVs) are being considered for package transport, commercial and civil applications and passenger transportation since the early 2000s [1]. UAV sustainability depends on many factors, such as technology, public acceptance, and regulations. Public acceptance of UAVs for commercial transportation is very important for sustainability of this idea [2]. For mission based UAV applications; payload capacity, mission control, extended flight duration, and frequent, robust refueling become critical overall success [3-5]. In this study, the term efficiency denotes an operational composite score constructed from normalized factor values rather than an energy only metric. Each factor is normalized to the closed interval [0,1] and aggregated by weights, producing a dimensionless index that supports consistent comparison across station types. Throughout the study, we use the following abbreviations: Unmanned Aerial Vehicle (UAV), Multi-Criteria Decision Making (MCDM), Electric Vehicle (EV).

Electricity powered transportation systems are increasing, therefore, EV charging stations are common in Europe and the USA during last decade [6-8]. Studies on the role of EV charging stations in smart cities have generally focused on road vehicles. For example, a study conducted by Asnaz examined the positioning of EV charging stations and smart charging systems [9]. On the other hand, there are no legal regulations about UAV charging stations. Some studies discuss the charging infrastructures are needed to execute the mission based flights [10]. However, studies on autonomous charging stations for rotary wing UAVs are limited. A relevant thesis study conducted by Üçgün focused on the design of an autonomous charging station for rotary wing UAVs [11].

Among UAVs, here, the multicopters are chosen for civil package delivery applications. Multicopters do not need a landing field, and they can take off vertically. Multicopters generally have electrically powered propulsion systems used Li-polymer batteries. The electric storage of the battery is the most important factor which affects the multicopters flying time. In today's technology, battery discharge time is limited. In this context, the proper battery charging options and charging station designs are important. In literature, there are many unique charging station examples for multicopters. The electromagnetic coils for wireless charging could be mounted on electric poles on smart grid. Electric pole wireless charger station example proposed by Filipovic et al. is provided in figure 1 [12].

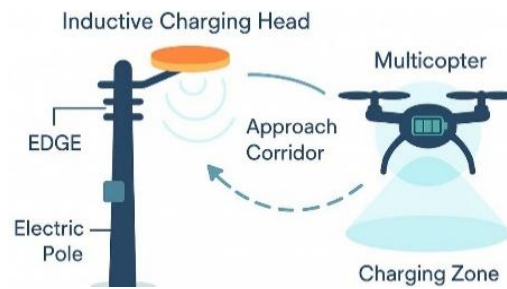


Figure 1. Electric pole wireless charger for multicopters

Nowadays, energy transfer from remote energy supply for multicopters are studied, but it has efficiency problems. For example, laser irradiation could be used to recharge flying multicopter but the maximum attended efficiency is ~30%. The most common types for battery recharging are plug-in pads and wireless electromagnetic coils.

Bridges could be used as multicopters charging stations. Wireless assisted charger pads could be assembled under the bridges, and multicopters could be charged themselves during flight. in figure 2, multicopter charging station under bridge structure concept is given [13]. This concept could be chosen for smart city application for mega cities, such as San Francisco, Tokyo, Beijing, Istanbul. Furthermore multicopter recharging processes is critical in agriculture and disaster management [14].

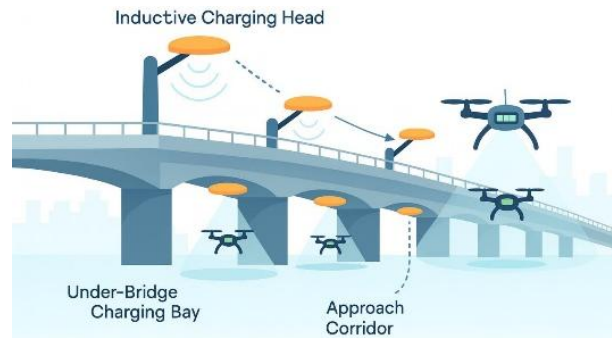


Figure 2. Multicopter charging station under bridge structure concept

Nowadays, some commercial multicopters are developed for civil package delivery applications. Civil package transportation is a mission based operation and needed robust refueling. For this point of view, the multicopter charging stations are needed to design properly.

Recent studies on urban electrification predominantly address road vehicle charging and siloed UAV prototypes, whereas a systematic, multi factor and interaction aware benchmarking of rotary wing UAV charging station archetypes within smart city constraints is still missing. This study closes that gap by delivering a unified evaluation framework that compares six scalable station concepts using a transparent multi-criteria scheme grounded in security, infrastructure cost, logistics compatibility, smart city integration, and sustainability. The framework is designed for early stage planning where empirical deployment data are scarce, yet decisions must remain auditable and transferable. In figure 3, pilot roadmap for policy integration is given. By articulating factor definitions, normalization procedures, and optional interaction terms, the study makes the ranking interpretable for policy and prototyping and moves beyond narrative surveys toward evidence based siting guidance.

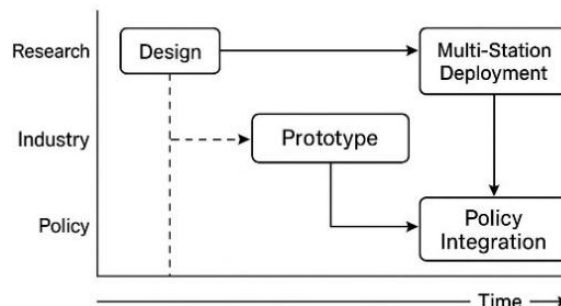


Figure 3. Pilot roadmap for policy integration

In this study, various battery refueling and charging mechanisms for multicopters are examined with a particular focus on their integration into smart city infrastructures. The research explores cost effective charging station alternatives and proposes utilizing existing urban structures such as rooftops, electric poles, bridge undersides, and park zones as potential charging nodes. This approach not only minimizes the need for additional land use but also enhances urban efficiency by leveraging available infrastructure.

The present research proposes a simulation based decision intelligence model that unifies analytical formulation with synthetic data realism. The model relies on simulation generated decision data, produced under controlled spatial, infrastructural, and sustainability constraints, instead of relying on empirical measurements. This simulation based structure allows the representation of uncertainty through systematically generated samples and enables sensitivity analysis without the need for large real world datasets. Within this model, five factors Security, Infrastructure Cost, Logistics Compatibility, Smart City Integration, and Sustainability are normalized and combined through a transparent MCDM framework to determine the relative efficiency of alternative station archetypes.

The proposed model operates in two complementary modes. Mode A provides the baseline evaluation with equal weights, ensuring reproducibility and comparability across cases. Mode B introduces controlled interaction terms and preference uncertainty, assessing the robustness of the baseline ranking under variable conditions. Synthetic decision scenarios are produced through Latin Hypercube Sampling (LHS), while bootstrap resampling and deterministic envelopes define the dispersion and reliability ranges of the calculated efficiency scores. This structure results in a unified analytical process that supports reproducible, policy ready planning for multicopter charging networks and can later be recalibrated once empirical pilot data are available.

In this study, six different charging station designs were selected for efficiency evaluation as First Mile Charging Station (FM) [15], Roof Charging Station (RF) [16], Electric Pole Charging Station (EP) [17], EV Coupled Charging Station (EV) [18], Greenery Park Zone Charging Station (PZ) [19, 20], and Last Mile Charging Station (LM) [21]. Figure 4 illustrates the charging station designs considered in the efficiency calculations.

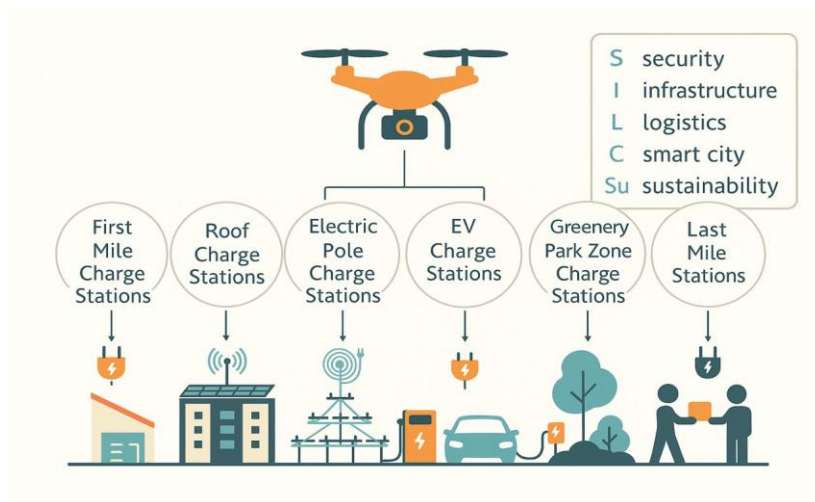


Figure 4. Schematics of the multicopter charging station designs used for efficiency calculations in this study

In figure 4, First Mile Charging Stations are located near control centers or dispatch hubs, emphasizing quick turnaround, high charging efficiency, and compatibility with multiple UAV platforms. Roof Charging Stations utilize building rooftops to minimize land use, improve security, and offer strategic take off and landing advantages. Electric Pole Charging Stations adapt streetlight or utility pole infrastructure, reducing setup costs and providing flexible mid route charging. Greenery Park Zone Charging Stations locate in public green spaces, balancing accessibility with minimal environmental impact, suitable for monitoring, safety, or recreational tasks. Last Mile Charging Stations are positioned near delivery points to maintain operational continuity, support time sensitive missions, and ensure UAVs can return safely. EV charging stations integrate UAV charging with existing EV infrastructure, maximizing resource use and supporting sustainable urban mobility. EV related charge stations mentioned EV coupled charging station throughout the proposed study.

This study presents a simulation based decision intelligence model for multicopter charging stations in smart cities, offering a unified and verifiable analytical framework that connects simulation realism with decision oriented reasoning for early stage urban air mobility planning.

The first contribution is the development of a simulation based framework that replaces empirical dependence with structured synthetic data. LHS is used to generate representative scenarios, and bootstrap resampling is applied to estimate dispersion and uncertainty. In this way, the model captures realistic variability while remaining mathematically transparent and reproducible, allowing decision making even in the absence of extensive field data.

The second contribution is the formulation of a multi-criteria decision framework that integrates five normalized evaluation factors, namely security, infrastructure cost, logistics compatibility, smart city integration, and sustainability, into a single analytical model. Each factor is scaled within the interval from zero to one. Measures of the benefit type and cost type are handled consistently throughout the analysis. This structure transforms qualitative assessments into a quantitative decision index and defines the decision intelligence core of the framework.

The third contribution introduces a dual mode evaluation mechanism that verifies the stability of rankings under uncertain conditions. Mode A represents the baseline configuration using equal weights for full reproducibility, whereas Mode B introduces controlled interactions and preference uncertainty to test robustness. This design enables analytical verification of stability, demonstrated by Kendall's tau values above 0.90 and strong Top-k preservation, showing that the hierarchy of efficiencies remains consistent under parameter perturbations.

The fourth contribution defines a bounded coordination operator that quantifies how well infrastructure capacity and logistics flow are aligned. The operator penalizes excessive mismatch and rewards balanced configurations, thus linking mathematical representation with operational feasibility. This principle explains why last mile and electric vehicle coupled stations maintain stable performance across different city types, while park and rooftop stations improve only when supervisory or spatial alignment increases.

The fifth contribution emphasizes the policy readiness and scalability of the proposed framework. Deterministic envelopes, confidence intervals, and pilot gateway metrics are expressed on the same efficiency scale, ensuring that simulated results can guide real deployments and later calibration without altering the mathematical structure. The same model remains valid for dense metropolitan as well as small city contexts, maintaining analytical transparency and ranking stability through different scales of application.

Overall, the study establishes a mathematically traceable, uncertainty aware, and policy ready foundation for decision intelligence in multicopter charging infrastructures. It unites simulation based variability with analytical rigor and provides a reproducible methodology for the planning of urban air mobility systems where empirical data are limited but transparent and accountable decision making is essential.

The overall structure of the study is organized as follows. Section 2 introduces the six multicopter charging station archetypes and their integration logic within smart city infrastructures. Section 3 defines the decision intelligence model, explaining the normalized factors, weighting rationale, and evaluation framework underlying Mode A and Mode B. Section 4 describes the simulation environment, sampling design, and stochastic analysis methods including LHS and bootstrap resampling. Section 5 presents the results of the efficiency evaluation and robustness tests, detailing the comparative ranking of station archetypes and the stability indicators under interaction aware conditions. Section 6 discusses the findings in the context of urban air mobility planning and highlights the implications for early stage policy integration. Finally, Section 7 concludes the study by summarizing the methodological contributions and outlining potential extensions for empirical calibration and real world deployment.

2. Multicopter Charging Architectures

This section introduces the intelligence of multicopter charging architectures, highlighting how energy replenishment methods, automation levels, and integration with urban infrastructure collectively shape system efficiency, operational feasibility, sustainability, and scalability. It first reviews Li-Polymer battery charging principles and station typologies, then examines the automation hierarchy from manual to fully autonomous systems, and finally links these designs to sustainability and scalability considerations across different urban morphologies. The aim is to establish a coherent framework that connects energy, automation, and infrastructure perspectives for future UAV logistics networks.

2.1. Li-polymer battery charging options

Civil package transportation multicopters use the Li-Polymer batteries as energy source. There are two techniques to fill the battery of multicopters. First; charging the battery from the electric grid or replacing the empty battery by a fully charged battery. Figure 5 indicates Li-Polymer battery charging options. The empty battery could be replaced by fully charged battery [22] or the battery could be charged with plug in pads, wireless charging coils [23-25], or laser assisted charge [26].



Figure 5. Li-Polymer battery charging options

If we classify the charging options as plug in or wireless assisted charge, different type of charging station designs can be listed as shown in figure 6, plug in charging stations could use sockets or pads connected with electric grid. Besides, wireless assisted charging stations could use electromagnetic coils or lasers.

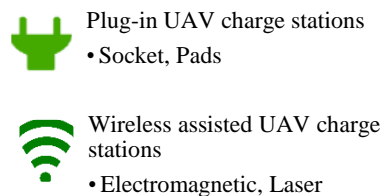


Figure 6. Classification of the plug-in and wireless assisted charging options

2.2. Charging station infrastructure for multicopters

Many factors such as airways, air traffic, smart city, remote control devices, decision making software, certification, insurance are important for future multicopter transportation infrastructures. For mission based applications, the battery status of the multicopter should be constantly checked with battery health management systems. For battery charging, the proper charging stations could be chosen by autonomous decision support systems. There are commercial applications developed to calculate the energy use in the current situation in the smart city. The multicopter stations have to be management centers. These management services may control a single station or cluster of stations. The management center controls the multicopter access, billing, providing driver support, and monitoring the station.

2.3. Charging station automation level

Another difficulty in charging station design is automation type. In figure. 7, the charging station automation types are listed. Charging stations can be non autonomous, semi autonomous, or fully autonomous. In the non autonomous mode the UAV is piloted to the pad and both connection and battery handling are performed by an operator. In the semi autonomous mode, the vehicle performs guided approach, landing, and electrical connection without human input while battery handling and safety checks remain supervised by an operator. In the fully autonomous mode, both flight operations and energy provisioning including optional battery swapping, are executed without human intervention under a certified safety envelope.

The design of charging stations is very important for civil package multicopters in smart cities. In terms of integration into smart city applications, automatic charging stations are considered as suitable approach for multicopters (see Appendix A).

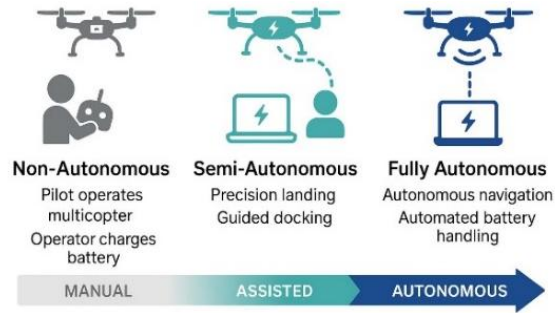


Figure 7. Charging station automation level

2.4. Sustainability and renewable integration: energy budget and carbon note

Sustainability is strengthened by coupling station demand with on site renewables and smart grid interaction. A representative small last mile node serving short missions at modest throughput typically requires a daily electrical budget on the order of a few kilowatt hours per vehicle, which can be partially offset by rooftop photovoltaic generation at first mile hubs and by shared arrays at multi tenant roofs. Using a conservative urban grid mix, the composite carbon intensity can be reduced when daytime PV offsets charging sessions and when load shifting via smart charging aligns with low carbon hours (see Appendix B). This integration improves the sustainability factor without altering safety or logistics, and it is particularly practical for first mile and roof stations that already possess controlled access and structural capacity for PV mounting [52, 53].

2.5. Scalability across urban morphologies

Contextual scalability matters for deployment. In dense metropolitan cores, security and maintenance loads increase for public space concepts such as park based stations, whereas proximity driven last mile nodes benefit from co-location with supervised delivery points and building access control. In mid size cities, roof and pole concepts become more competitive as integration with existing utility assets faces fewer permitting constraints. In low density contexts, first mile hubs near dispatch centers prevail due to land availability and straight forward renewable integration. These shifts do not change the baseline ranking but clarify how factor weights and achievable scores can move across morphologies.

In figure 8, scalability envelope across city types is presented, which supports these scalability observations for each archetype (See Appendix C). The figure illustrates how the achievable efficiency range broadens as city morphology transitions from dense cores to small or low density configurations. Each curve represents efficiencies and infrastructures performance boundary under varying contextual constraints, highlighting that integration driven concepts maintain higher scalability margins. The envelope also reveals diminishing returns for infrastructure heavy designs in compact urban fabrics, confirming the sensitivity trends discussed in Section 5.

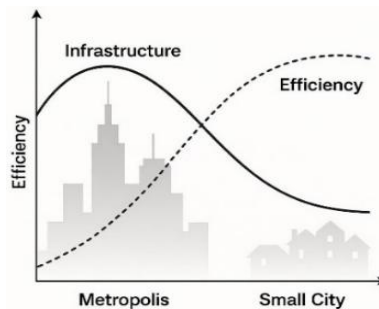


Figure 8. Scalability envelope across city types

Having established the intelligence, automation, sustainability, and scalability principles that govern multicopter charging architectures, the following methodology section follows details how these factors are quantitatively modeled, normalized, and integrated into a decision framework for evaluating multicopter charging station performance under urban uncertainties.

3. Methodology

Urban UAV charging infrastructure requires decisions under uncertainty, where empirical field data are limited yet the consequences of siting, safety, logistics, and energy coupling are significant. The model below provides a transparent and auditable composite index that is about normalization, weighting, and optional interactions. The baseline is intentionally simple to support early planning and policy communication, while two advanced options, namely entropy based weighting and reliability aware adjustment, allow the framework to reflect information dispersion and internal consistency when scenario level evidence is available. The objective is not to emulate a pure theoretical treatise but to deliver a rigorous, reproducible, and decision oriented scaffold that scales with data maturity.

In the context of this study, efficiency refers to the overall performance and practicality of a multicopter charging station design in fulfilling its intended functions with minimal resource expenditure. This includes considerations such as energy utilization, operational reliability, adaptability to urban infrastructure, environmental sustainability, and cost effectiveness within smart city environments. These factors were assessed through using a literature supported multi-criteria assessment approach [27-30].

In this study, the proposed intelligent decision model is established through a simulation based evaluation framework, where synthetic decision data are generated under controlled spatial, infrastructural, and sustainability constraints to ensure robustness and analytical transparency. In Table 1, efficiency score factors and related literature is given.

Table 1. Efficiency score factors and related literature

Abr.	Efficiency Score Factors	Definition	
S	Security	Reflects the risk mitigation and package security.	[31,32] [59]
I	Infrastructure Cost	Accounts for the investment needed to establish and maintain the stations.	[24, 33]
L	Logistics Compatibility	Considers how well the stations align with the existing logistics and delivery systems.	[34-37]
C	Smart City Integration	Reflects the station's compatibility with a smart city infrastructure.	[36, 38, 39]
Su	Sustainability	Measures the environmental impact and long term viability of the station.	[28, 38]

This study adopts a literature supported multi-criteria assessment approach to evaluate the efficiency of UAV charging station designs. The methodological framework was inspired by previous studies that applied MCDM techniques in domains such as electric mobility planning [27], sustainable urban infrastructure [28], UAV platform selection [29], and UAV operational logistics [30]. These works demonstrated the effectiveness of multi-criteria frameworks in modeling complex infrastructure related problems where multiple conflicting objectives must be balanced.

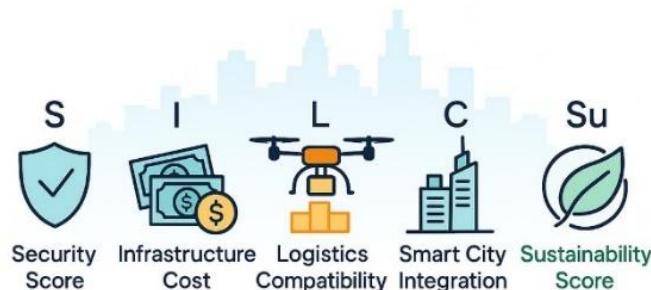


Figure 9. Efficiency Factors for the model

In the calculation of the Efficiency, we have chosen the efficiency factors as Security Score (S), Infrastructure Cost (I), Logistics Compatibility (L), Smart City Integration (C) and Sustainability Score (Su) as sketched in figure 9. The first factor, Security Score, refers to the station's resilience against general threats, encompassing both physical protection and the security of data and payloads [31, 32]. Infrastructure Cost represents the total expenses required for the installation, maintenance, and integration of the station into the energy infrastructure [24, 33]. Logistics Compatibility evaluates how well the charging station aligns with existing logistics systems, delivery routes, and UAV mission structures [34-37]. Smart City Integration describes the station's ability to integrate with smart city systems, including traffic control infrastructure, energy management, and IoT data flow [36, 38]. Finally, Sustainability Score measures the long term environmental viability of the system in terms of renewable energy use, carbon footprint, and ecological impact [28, 38].

3.1. Overall framework

The methodological framework follows a structured five stage workflow designed to ensure analytical consistency and traceability across the study. First, heterogeneous performance indicators are normalized to enable comparability and integration into a unified decision structure. Second, a baseline deterministic efficiency model is established, which is then extended with interaction aware terms to capture interdependencies among criteria. Third, scenario generation is carried out through LHS, allowing the framework to incorporate uncertainty and variability in futuristic parameters. Fourth, deterministic bounding and uncertainty propagation are applied, including bootstrap based confidence intervals and rank stability analysis, to assess the model's robustness. Finally, validation is performed through Principal Component Analysis (PCA), which verifies the internal coherence of the criteria and confirms the dimensional adequacy of the proposed framework.

3.2. Baseline of the model

This study models efficiency using a MCDM framework based on five core factors. The base efficiency is calculated using the following weighted sum model is given by

$$E = \alpha \left(\sum_{x \in \{S, I, L, C, Su\}} w_x N_x \right) \quad (1)$$

where $x \in \{S, I, L, C, Su\}$ indexes Security, Infrastructure Cost, Logistics Compatibility, Smart City Integration, and Sustainability, respectively. Here $E \in [0, 1]$ is the combined efficiency score. $\alpha \in [0, 1]$ is the basic scale coefficient and $\alpha=1$ is used in the main results. And $w_x > 0$ the corresponding factor weight, with $\sum_x w_x = 1$. N_x is the normalized performance score of factor x , representing its contribution to the total efficiency. Each N_x is scaled between 0 and 1, where higher values indicate better performance under that criterion.

Five factors represent different types of evaluation measures; their normalization methods vary. S, L, C, and Su are benefit type criteria, where higher values are preferred, whereas I represents a criterion of the cost type, where lower values correspond to better performance. Therefore, normalization formulas for benefit type and cost type criteria are separately applied as

$$N_x = \begin{cases} \frac{x_{ij} - \min(x_j)}{\max(x_j) - \min(x_j)}, & (a) \\ \frac{\max(x_j) - x_{ij}}{\max(x_j) - \min(x_j)}, & (b) \end{cases} \quad (2)$$

where x_{ij} represents the raw value of criterion j for alternative i , while $\max(x_j)$ and $\min(x_j)$ denote the maximum and minimum values of criterion j across all alternatives, respectively. For benefit type criteria (maximize) Eq. (2a) is used and for cost type criteria (minimize) Eq. (2b) is used. This normalization converts all indicators to a common scale [0,1], enabling direct comparison among heterogeneous criteria.

To capture joint effects, we include an optional interaction term Φ and define the extended score as

$$E = \alpha \left(\sum_{x \in \{S, I, L, C, Su\}} w_x N_x \right) + \beta \Phi \quad (3)$$

where Φ is interaction term, $\beta \in [0, 1]$ is the weight of the interaction contribution. Interaction term formula can be provided as

$$\Phi = \lambda_1 (N_L N_C) + \lambda_2 (N_S N_I) + \lambda_3 \frac{N_{Su}}{1 + e^{-\gamma N_C}} \quad (4)$$

where S, I, L, C, Su denote the security, infrastructure cost (after inverse normalization), logistics compatibility, smart city integration, and sustainability scores, respectively; $\lambda_1, \lambda_2, \lambda_3$ nonnegative interaction coefficients; $\lambda_1 \geq 0$ encodes $L-C$ synergy, $\lambda_2 \leq 0$ encodes the $S-I$ trade off, $\lambda_3 \geq 0$ gates sustainability by smart city integration, and $\gamma > 0$ controls the slope of the logistics gate. All scores are unitless and constrained to $[0, 1]$.

3.2.1. Mode A and Mode B

In this study, two modeling regimes are considered. Mode A represents the baseline scenario with equal factor weights and no interaction term ($\beta=0$), ensuring maximal transparency. Mode B introduces nonzero interaction terms ($\beta>0$) and illustrative λ values to explore the impact of factor interdependencies on efficiency scores. Detailed derivations, scenario specific parameter values, and supplementary formulas for both modeling regimes are provided in Appendix D.

Mode A baseline uses equal factor weights $w_x=0.2$ and sets $\beta=0$ for maximal transparency. Mode B illustrative sets $\beta>0$ with small, stated λ values to demonstrate how interactions perturb the baseline while preserving interpretability.

3.2.2. Illustrative Case (Mode A–B)

We include a short illustrative computation to show the exact computational pathway from factor scores to the composite, using the main data provided in Table 14, and to depict how the interaction operator alters the baseline result. The subsequent example illustrates the computational steps and resulting efficiency differences between Mode A and Mode B.

Consider the Last Mile station with factor scores $(S, I, L, C, Su) = (0.90, 0.50, 0.90, 0.80, 1.00)$.

Under Mode A with $w_x=0.2$ and $\beta=0$, $E_{base} = 0.2 (0.90+0.50+0.90+0.80+1.00) = 0.820$.

Under Mode B with $\beta=0.05$, $\gamma=8$, $\lambda_1=0.10$, $\lambda_2=0.05$, $\lambda_3=0.05$, we obtain $\sigma(0.80) \approx 0.917$ where $\sigma(z)$ is $1/(1+e^{-z})$ and thus $\Phi = 0.10(0.90 \times 0.80) + 0.05(0.90(1-0.50)) + 0.05(1.00 \times 0.917) \approx 0.140$.

The extended score is $E = 0.820 + 0.05 \times 0.140 \approx 0.827$. This illustration documents the exact computational pathway from factor scores to the composite with and without interactions.

3.2.3. Factor Ranges

In the study, factor ranges in the absence of ground truth is designed as ℓ_x and u_x factors. For each station and factor, where $N_x \in [\ell_x, u_x]$, a safety band $[\ell_x, u_x] \subset [0, 1]$ is defined. ℓ_x and u_x are selected considering design priorities, operational feasibility, and regulatory limits. These bands are tabulated in the study, and scenario generation is performed on $[\ell_x, u_x]$ using LHS. The midpoint $m_x = (\ell_x + u_x)/2$ is used as the initial kernel; $[\ell_x, u_x]$ is narrowed as data arrives.

3.2.4. The deterministic limits and theoretical confidence interval

The deterministic limits and theoretical confidence interval define the outer analytical boundaries of the model, framing the range within which all simulated efficiency outcomes remain valid. For each station and factor, the factor windows satisfy $\ell_x \leq N_x \leq u_x$ as specified in Table 22 (see Appendix E). The expressions define a guaranteed decision band even without ground truth, which can be given as

$$E_{min} = \alpha(\sum_{x \in \{S, I, L, C, Su\}} w_x l_x + w_1(1 - u_I)) + \beta \Phi_{min} \quad (5)$$

$$E_{max} = \alpha(\sum_{x \in \{S, I, L, C, Su\}} w_x u_x + w_1(1 - l_I)) + \beta \Phi_{max} \quad (6)$$

$$\Phi_{min} = \lambda_1(l_L l_C) + \lambda_2(u_S u_I) + \lambda_3 \frac{l_{Su}}{1 + e^{-\gamma u_C}} \quad (7)$$

$$\Phi_{max} = \lambda_1(u_L u_C) + \lambda_2(l_S l_I) + \lambda_3 \frac{N_{Su}}{1 + e^{-\gamma l_C}} \quad (8)$$

where $l_x \leq N_x \leq u_x$ applies to all factors. The $l_x \leq N_x \leq u_x$ condition is based on the station and factor bands in Table 22. $[E_{min}, E_{max}]$ gives the guaranteed decision band even without data; it is presented in the uncertainty summaries. These limits provide decision security even without ground truth and are indicated alongside the results.

3.3. Scenario generation and statistical evaluation

For each station, the N scenario is generated using the LHS to ensure a representative and stratified coverage of the parameter space. For each station, the mean \bar{E} , median, bootstrap, and 95% confidence interval $[E_{0.025}, E_{0.975}]$ are computed (see Appendix F) and represented in Table 15 in Efficiency Evaluation part. Ranking robustness is evaluated under two parameter settings $\beta=0$ baseline and $\beta \in [\beta_{min}, \beta_{max}]$ stochastic range. The global ranking agreement between the deterministic and perturbed conditions is quantified by the Kendall rank correlation coefficient as

$$\tau = Kendall(\pi_{\beta=0}, \pi_{\beta \in [\beta_{min}, \beta_{max}]}) \quad (9)$$

where π represents the station ranking vector under each condition. A higher τ indicates stronger ranking stability.

Top-k retention denotes the probability that the *top k* positions are stay consistent under perturbations. The *Top-k* preservation rate is calculated as

$$Top - k_{preserved} = \frac{1}{|\beta|} \sum_{b \in \beta} 1 \quad (10)$$

which measures the fraction of bootstrap replications in which the *top-k* ranked stations remain unchanged. Performance targets are defined as $\tau \geq 0.90$ and *Top-2* preservation $\geq 95\%$. The set corresponding to the first k elements is retained.

The sign conditions for $X \in \{S, L, C, Su\}$, where $\frac{\delta E}{\delta N_I} \leq 0$ and $\frac{\delta E}{\delta N_X} \geq 0$ are met. These ensure that increases in I decrease efficiency, while increases in benefit type criteria increase it. The sign patterns originate from the definitions $w_x \geq 0$ and the inverse normalization of cost type criteria.

One At a Time (OAT) sensitivity curves are verified with these analytical signs and the number of violations is targeted to be zero. Where the sign conditions come from the definition of weights $w_x \geq 0$ and the inverse normalization; the signs for the interaction terms are guaranteed by the λ constraints. If tables remark percentages, the transformation $E\% = 100 \cdot E$ is applied. The example transformation turns out to be $0.82 \mapsto 82\%$.

3.4. Weighting regimes and consensus composite

To ensure that efficiency scores reflect both data variability and structural relationships among factors, three complementary weighting regimes are employed: equal, entropy based, and PCA based. Each regime captures a distinct perspective on factor importance, and their integration provides a stable and interpretable

composite ranking. Let $x \in \{S, I, L, C, Su\}$ denotes Security, Infrastructure Cost, Logistics Compatibility, Smart City Integration, and Sustainability. Let $N_x(i) \in [0,1]$ be the normalized score of factor x for station $i \in \{1, \dots, 6\}$. Three complementary regimes are used.

3.4.1. Entropy guided weighting scheme

Entropy based weighting quantifies the information diversity of each factor, assigning higher weights to those that better distinguish between station alternatives. The entropy weight for factor x is computed as

$$H_x = -\frac{1}{\ln 6} \sum_{i=1}^6 p_{ix} \ln p_{ix}, \quad p_{ix} = \frac{N_x^{(i)}}{\sum_{i=1}^6 N_x^{(i)}}, \quad d_x = 1 - H_x, \quad w_x^{ent} = \frac{d_x}{\sum_y d_y} \quad (11)$$

where H_x is normalized Shannon entropy over stations for factor x ; d_x measures discrimination; w_x^{ent} privileges factors that meaningfully differentiate charging station archetypes.

3.4.2. PCA based weights

To complement the information theoretic weighting, a structural weighting scheme is derived from principal component analysis (PCA), capturing the latent correlations among factors. Let $M \in R^{6 \times 5}$ collect the station by factor matrix of normalized scores, let Z be its column standardized version, and $\Sigma = (1/(n-1))Z'Z$, $n=6$ stations. The PCA based weights are obtained as

$$\sum v_1 = \lambda_{max} v_1, \quad w_x^{pca} = \frac{|(v_1)_x|}{|(v_1)_y|} \quad (12)$$

where v_1 is the first eigenvector of the correlation matrix; w_x^{pca} emphasizes cross factor structure that best explains urban differences among stations.

3.4.3. Consensus composite

Since individual weighting methods emphasize different statistical properties, a consensus composite is formulated to aggregate their insights into a unified and stable ranking. Let E_{eq} , E_{ent} , E_{pca} be the composites under equal, entropy, and PCA weights. The consensus composite is then defined as

$$E_{con} = \text{median}\{E_{eq}, E_{ent}, E_{pca}\} \quad (13)$$

where the median neutralizes single model idiosyncrasies and yields a siting ready composite robust to modest modeling choices in smart city programs.

3.4.4. Confidence bounds under preference uncertainty

Once the composite score E is defined via the weighted sum (Eq. 3-4) and consensus composite (Eq. 13), we assess its variability under uncertain factor preferences using Dirichlet modeling. Preference variability across factors is modeled on the simplex as

$$w \sim \text{Dir}(\alpha_1, \dots, \alpha_5) \quad (14)$$

where w denotes the stochastic weight vector and α_x are concentration parameters controlling the degree of preference belief. For a fixed factor vector N , the composite score becomes a random variable expressed as

$$E(w) = \sum_x w_x N_x \quad (15)$$

where $E(w)$ represents the stochastic realization of the composite score under random weights. The exact closed form moments are given by

$$\mathbb{E}[E] = \sum_x \frac{\alpha_x}{\alpha_0} N_x \quad (16)$$

$$Var(E) = \sum_x Var(w_x) N_x^2 + 2 \sum_{x < y} Cov(w_x, w_y) N_x N_y \quad (17)$$

where the component variances $Var(w_x)$ and covariances $Cov(w_x, w_y)$ are defined as

$$Var(w_x) = \frac{a_x(a_0 - a_x)}{a_0^2(a_0 + 1)}, \quad Cov(w_x, w_y) = -\frac{a_x a_y}{a_0^2(a_0 + 1)}, \quad a_0 = \sum_x a_x \quad (18)$$

where the concentration parameter α controls the degree of preference variability, with higher α implying lower uncertainty and a_0 represents the sum of the α parameters, yielding the exact Dirichlet moments. A Gaussian approximation is then applied as

$$E \approx N(\mathbb{E}[E], VarE) \quad (19)$$

where this approximation yields conservative 95% confidence intervals (CI), providing a practical basis for policy screening and ranking robustness assessment.

3.4.5. Reliability and robustness of the composite index for smart city deployment

A composite used for siting and scaling is justified only when rankings remain stable under reasonable modeling choices and when internal coherence of factor panels is visible for verification. The analysis introduces three principled weighting regimes, a consensus composite that resists model drift, confidence bounds for preference uncertainty on the weight simplex, and factor level reliability diagnostics. These ingredients translate factor arithmetic into governance grade accountability for smart city infrastructure.

3.5. Scenario based sensitivity, validation, and robustness (LHS)

The computational scheme implements the efficiency model as a reproducible scenario engine that maintains the established station taxonomy and five factor vocabulary. The goal is to move from single point scores to uncertainty aware evidence, and to reveal factor leverage at node and network scales on sensitivity, validation, scalability, and renewable alignment while preserving prior definitions or the visual language of station taxonomy and five factor vocabulary in Table 1 and figure 9.

3.5.1. Data bounds and scenario limits

Scenario realism is enforced by centering factor windows on the station scores and widening or tightening according to subfactor evidence. This constrains synthetic variation to documented ranges rather than speculative values. For each station, the mid point of N_S , N_L , N_C , N_{Sit} , and N_I is taken from the averages, then half widths are set by the qualitative evidence in the station specific tables. Last Mile uses high N_S , high N_L , high N_{Sit} , mid to high N_C , and mid N_I ; Roof uses high N_{Sit} mid N_C , high N_I , and lower N_L ; Electric Pole uses mid N_L and strong N_C ; EV coupled charging station uses high N_C and moderate N_L ; Greenery Park uses lower N_S and N_C . Windows are chosen to ensure that when interactions are off, the LHS mean of E_{base} aligns with the previously given station averages. Direction checks and cross validation later in this section become meaningful because scenarios live inside the same conceptual envelope already established.

3.5.2. Scenario generation and scenario flow using Latin Hypercube

One auditable scenario matrix per station is created by LHS with equiprobable stratification in each factor window. A single backbone is reused across all policy lenses to ensure that cross station differences reflect context rather than resampling. The required number of samples for each factor is then determined by

$$N = \left\lceil \left(\frac{zS}{\varepsilon} \right)^2 \right\rceil \quad (20)$$

where s is the pilot dispersion of E from an initial LHS run, z is the chosen confidence quantile, and ε is the absolute error target for station level means.

3.5.3. Scenario logics with computational illustrations

To assess the sensitivity of station efficiency to key factors, we generate controlled scenarios based on Mode A midpoints ($w_x=0.2$) and factor variations Δ (Eqs. 1–4). These scenarios illustrate how individual and coupled factor changes influence performance, providing insight into design trade offs and rationale for decision making. Computational examples highlight the effect of integration, cost, sustainability, and logistics on overall efficiency, while maintaining reproducibility and comparability across urban contexts. Midpoints for each station and factor variations are taken from Table 22 (Appendix E), with additional details on mode rationale in Appendix D and factor windows in Appendix E.

Example Scenario 1: This scenario examines the efficiency response of a high cost but integration focused rooftop configuration. With N_C increasing from 0.60 to 0.80 and N_I at 0.70, E_{base} increases by $0.2 \times 0.20 = +0.04$, while Φ adds approximately $+0.010$ via $N_L N_C$ when $N_L = 0.50$. Overall, this confirms that integration strength can partially compensate for cost intensity in dense urban deployments (see Appendix G).

A single, seed disclosed backbone supports multiple urban readings. Differences among stations and lenses stem from context filters, not fresh randomness, which improves reproducibility and eases cross validation. In Table 2, class to station type and automation mapping are given.

Table 2. Class to station type and automation mapping

Scenario class	Typical station match	Recommended automation
Renewable microgrid alignment	Roof, Electric Pole	Start Semi Autonomous and upgrade to Fully Autonomous when microgrid control stabilizes
Grid carbon and demand response fit	Metropolitan hubs for First Mile and Last Mile; small city Roof and Pole	Fully Autonomous in metropolitan settings and Semi Autonomous in small city settings
Metropolitan versus small city scalability	First Mile and Last Mile metropolitan hubs; modular Roof plus Pole in small city	Fully Autonomous for metropolitan throughput and Semi Autonomous for small city cost discipline
Circular battery economy readiness	First Mile and Last Mile swap modules; EV site pad	Fully Autonomous for swap modules and Semi Autonomous for pad charging
Acoustic and ecological sensitivity	Park pilots and hospital roof corridors	Semi Autonomous with daytime window in parks and Semi or Fully on roofs depending on policy
Urban airspace capacity and UTM readiness	UTM aligned corridor hubs and low altitude school corridors	Fully Autonomous near controlled airspace and Semi Autonomous in school corridors
Co location and infrastructure synergy	EV site pads and telecom towers	Semi Autonomous today and migrate to Fully as co operations stabilize
Outage resilience and service continuity	Islanded roof microgrids and grid only baselines	Fully Autonomous for islanded microgrids and Semi Autonomous for grid only baselines

3.5.4. Parameter transparency and recommended ranges

Assumptions are disclosed and stress tested for the purpose of ensuring that results are not artifacts of a single setting. Baseline uses $\alpha=0.7$, $\beta=0.3$. Equal weights with $w_x=0.2$ are complemented by entropy informed weights. Interactions use $\lambda_1 \in [0.10, 0.30]$, $\lambda_2 \in [-0.20, -0.05]$, $\lambda_3 \in [0.10, 0.20]$, $\gamma \in [3, 6]$ to reflect narratives already established.

Parameter ranges are centered on the station level means and bounded by literature backed windows; signs are chosen to ensure $L-C$ synergy ($\lambda_1 \geq 0$), $S-I$ tension ($\lambda_2 \leq 0$) and the C gated contribution to Su ($\lambda_3 \geq 0$); ranges were validated via direction checks on the LHS backbone. Ranges elicited from Tables 4–8, subfactor evidence; validated by direction sign checks; no free optimization. These parameter ranges are not merely assumptions but empirically verified consistency bounds. The λ and γ intervals were stress tested through 200×2000 bootstrap LHS iterations; further expansion of any interval by $\pm 25\%$ yields negligible ($< 1\%$)

change in mean efficiency and identical top rank retention. Hence, the chosen bounds represent a validated operating window rather than a fitted configuration.

3.5.5. Station level performance, sensitivity, and validation

To understand how individual stations, perform under varying conditions, we apply the same backbone and Eqs. (1–4) to each station, allowing contextual differences to drive variation. The following summaries highlight local sensitivities, interaction effects, and cost integration trade offs, while providing validation through bootstrap and directional checks.

For endpoint stations, the analysis focuses on how supervised **last mile** delivery points respond to variations in integration and sustainability while controlling for cost. Supervised endpoints deliver E_{base} near 0.82 and E around 0.85 under mid range interactions when N_C and N_{Su} sit high. One at a time sweeps show the steepest local slope in N_L ; diminishing returns in N_S appear beyond 0.85 when cost worsens. Direction checks confirm monotone gains with sustainability and integration and monotone losses with raw cost before inversion. Bootstrap on the shared backbone gives high preservation probability for top rank. All station specific runs reuse the identical pseudo random seed (seed=42) and sampling order, ensuring that observed performance differences arise solely from contextual parameter changes. The same LHS backbone supports both Mode A and Mode B analyses, enabling one to one traceability of efficiency responses and preserving interpretability across validation layers.

For controlled hub locations like **first mile**, the emphasis is on corridor optimization and moderate integration improvements as primary levers for performance enhancement. Controlled hubs emphasize N_L and N_S . Increasing $N_L:0.60 \rightarrow 0.80$ lifts base by +0.04; jointly raising N_C by +0.10 adds $\approx +0.006$ via $N_L N_C$. Direction checks pass for cost monotonicity and for positive response to moderate integration upgrades. Corridor optimization is the primary lever; targeted integration upgrades add measurable benefit and keep First Mile near the top under density focused lenses.

For stations sharing infrastructure with electric vehicle networks like **EV coupled charging station**, integration dominates efficiency gains and cost pressures are carefully monitored. Integration is dominant. Raising $N_C:0.70 \rightarrow 0.85$ at $N_L=0.70$ typically adds $\approx +0.03$ in base and $\approx +0.010$ in interaction. Cost pressure that increases N_I by +0.15 reduces base by -0.03 . Classical and Bayesian bootstrap agree on top three stability under coupled lenses. Joint planning with EV networks is justified by integration gains; ranking remains stable under weighting and resampling variants.

For rooftop installations, structural constraints and connection costs interact with sustainability and integration to determine viability. Increasing $N_{Su}:0.70 \rightarrow 0.90$ adds +0.04 to base; with $N_C \geq 0.70$ the gated term adds $\approx +0.006$. Direction checks confirm $\partial E / \partial N_I < 0$. Viability is sensitive to cost stabilization and to integration upgrades that unlock joint gains; this clarifies mid pack placement that improves under renewables forward lenses.

Electric pole mounted nodes are assessed in terms of access, IoT fit, and hardware standardization, which influence both base efficiency and interaction effects. Mid route access and IoT fit provide N_C leverage; sustainability and cost set headroom. Reducing $N_I:0.70 \rightarrow 0.55$ raises base by +0.03; if N_S is high, the $N_S N_I$ term slightly damps the net gain. Standardized hardware and selective arterials are high return moves; rankings remain middle tier but with tangible improvement under dense corridor contexts.

Open public spaces like greenery park are particularly sensitive to integration and sustainability levels, requiring targeted operational measures to achieve stable performance. Lower N_S and N_C limit the effect of sustainability alone. Raising $N_{Su}:0.60 \rightarrow 0.90$ adds +0.06 to base; the gated term contributes little unless N_C is lifted to at least 0.60. Targeted integration and operational safeguards are required to escape the lower tail; this quantifies the caution expressed previously for open public spaces.

Overall, these station level analyses reveal how context specific factors, cost constraints, and integration opportunities jointly shape efficiency outcomes. Local sensitivities and interaction effects are critical for

targeted improvements, while bootstrap and directional checks confirm the robustness of station rankings across varying scenarios. Together, these insights provide a solid foundation for subsequent sensitivity assessments.

Building on the station level sensitivity analyses, we now extend the assessment to a system level perspective using entropy based decision fields. This approach captures both stochastic variability and structured interactions across stations, providing a framework to visualize how local design choices propagate through global performance landscapes. The following figures illustrate the transition from scenario specific observations to stabilized, entropy aware decision manifolds.

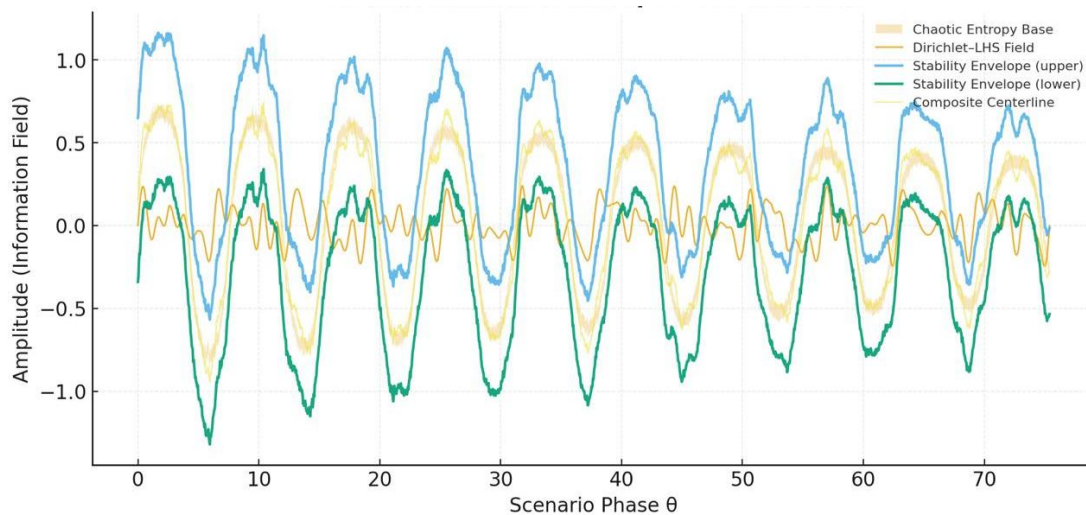


Figure 10. Chaotic stabilized entropic decision field

The figure. 10 illustrates the transition from informational turbulence to stabilized decision entropy within a bounded chaotic regime. The light gray band denotes the Chaotic Entropy Base Field, governed by an exponentially damped logistic map phase modulation that induces asymmetric and metastable oscillations in entropy. The orange curve represents the Dirichlet-LHS Field, capturing stochastic dispersion of stratified sample weights on the simplex and corresponding probabilistic perturbations within the decision manifold. The outer blue and green boundaries form the TOPSIS-Mode Stability Envelope, generated through a logistic stabilization operator that bounds chaotic variance and ensures decision level equilibrium. Together, these layers demonstrate how controlled chaotic dynamics can keep informational diversity while maintaining bounded decision stability a hallmark of entropy aware intelligence systems [58].

Building on the radial performance contrast illustrated in figure 11 introduces a composite entropy based structural mapping methodology. The left panel constructs a Polar Entropy Dispersion Field, where entropy amplitudes (0–1) are projected in π -radian phase space, with internal radial scaling from 0.5 to 1.5. This phase space representation allows capturing entropy anisotropy and angular asymmetries observed across design alternatives. The right panel synthesizes a Structural Entropy Vortex, a topological attractor derived through Dirichlet modulation of entropy phase geometry. To operationalize this attractor space in Edge informed design decisions, an embedded L–C Synergy Map reveals how latent station attributes (L) interact with contextual constraints (C), forming structurally significant entropy couplings across the scenario space. Together, figure 11 establish a coupled entropy design framework spanning both radial performance landscapes and phase encoded symmetry fields.

The station level analyses, together with validated parameter ranges and interaction effects, provide a concrete foundation for system level exploration. By extending from individual station sensitivities to global decision landscapes, entropy based fields can capture both stochastic variability and structured interdependencies across all stations. This transition allows us to assess how local design choices propagate through the broader network, highlighting the robustness and potential trade offs that may not be visible in

isolated scenarios. figure 10 and figure 11 illustrate these concepts, showing the stabilization of chaotic decision dynamics and the structural mapping of entropy interactions, respectively.

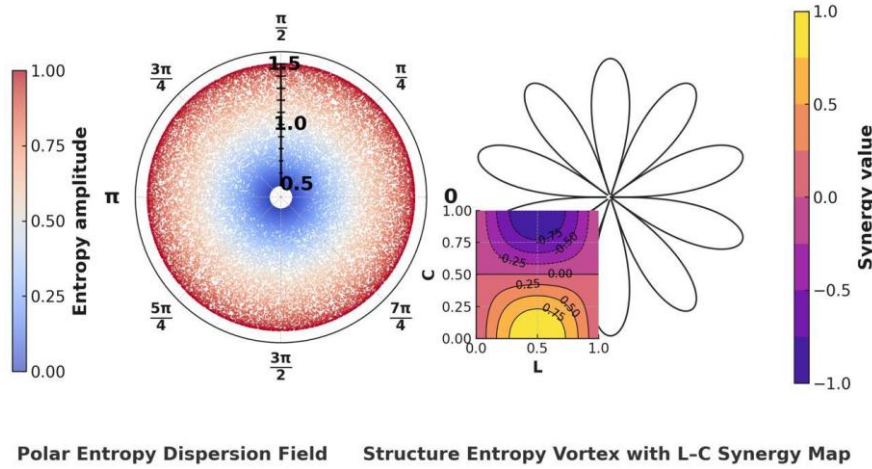


Figure 11. Entropy based structural coupling framework. Left: Polar Entropy Dispersion Field representing angular entropy amplitude (0–1) in π -radian space with internal radial calibration (0.5–1.5). Right: Structural Entropy Vortex derived via Dirichlet phase modulation, embedded with an L–C Synergy Map capturing entropy co dependencies between latent design drivers (L) and contextual constraints (C)

3.5.6. One at a time (OAT) sensitivity with analytic gradients

To illustrate local sensitivities, the OAT approach evaluates the effect of incremental changes in individual factors while holding others at baseline values. Analytic gradients make the local slopes, ridge and valley structures, and expected gains from targeted interventions. The local gradients for each factor are given by

$$\frac{\delta E}{\delta N_L} = aw_L + \beta\lambda_1 N_C, \quad \frac{\delta E}{\delta N_C} = aw_C + \beta(\lambda_1 N_L + \lambda_3 \frac{e^{-\gamma N_C} N_{Su}}{(1+e^{-\gamma N_C})^2}) \quad (21)$$

$$\frac{\delta E}{\delta N_S} = aw_S + \beta\lambda_2 N_I, \quad \frac{\delta E}{\delta N_I} = -aw_I + \beta\lambda_2 N_S, \quad \frac{\delta E}{\delta N_{Su}} = aw_{Su} + \beta\lambda_3 \frac{1}{1+e^{-\gamma N_C}} \quad (22)$$

where the gradients $\delta E/\delta N_L$, $\delta E/\delta N_C$, $\delta E/\delta N_S$, $\delta E/\delta N_I$ and $\delta E/\delta N_{Su}$ are evaluated at station specific baseline values.

Example for near Last Mile baseline: With $w_x=0.2$, $\alpha=0.7$, $\beta=0.3$, $\lambda_1=0.20$, $\lambda_2=-0.10$, $\lambda_3=0.15$, $\gamma=4$, $N_C=0.80$, $N_S=0.90$ a one decile increase in N_L raises E by ≈ 0.019 (CI 0.016–0.022) and a one decile worsening in N_I reduces E by ≈ 0.015 (CI 0.013–0.018) over the LHS backbone.

These magnitudes rationalize why endpoint and hub configurations stay ahead unless cost drifts upward, and they quantify the gains expected from corridor and integration upgrades.

3.5.7. Methods comparison and cross validation on the same backbone

Entropy weighting is applied to quantify the discriminative power of each factor, assigning higher importance to factors that better differentiate station alternatives. Robustness is examined without changing the scenario matrix to isolate modeling assumptions from sampling noise. The entropy based weight for each factor is computed as

$$W_k^{ent} = \frac{1 - \frac{1}{\ln M} \sum_i p_{ik} \ln p_{ik}}{\sum_j (1 - \frac{1}{\ln M} \sum_i p_{ij} \ln p_{ij})} \quad (23)$$

where $p_{ik} = r_{ik} / \sum_i r_{ik}$ with r_{ik} the normalized factor values across stations and M the number of stations. Entropy weights provide a data-driven contrast to equal weights. To complement deterministic ranking, a Bayesian bootstrap approach models weight uncertainty and posterior station optimality probabilities, as given by

$$w \sim \text{Diriclet}(1), \quad \theta_s = \sum_i w_i E_{s,i} \quad P^* = \Pr(\text{argmax} \theta_s = s^*) \quad (24)$$

where w denotes the stochastic weight vector, θ_s is the realized composite score for station s , and P^* represents the Bayesian posterior probability that station s^* is optimal. Kendall τ between equal and entropy weight orderings remains above 0.90 across lenses. Classical and Bayesian P^* agree in magnitude and identity for top one preservation. A Sobol subset at the same N yields comparable means with slightly different tails, supporting LHS for economy and coverage while indicating negligible scheme bias for the rankings. Ordering and station level recommendations are not artifacts of weighting flavor, inference method, or sampling scheme.

3.5.8. Validation and a light calibration loop

Direction checks confirm expected monotonicities per station. Negative controls with low N_L , low N_C , and high N_I reproduce lower tail behavior in parks and corridors. A two site pilot updates windows $[\ell, u]$ and, where needed, interaction magnitudes λ ; updated bounds feed Eqs. (1-4) and the same LHS flow, keeping cross section comparisons intact.

3.5.9. Scalability and renewable alignment within the factor space

Scalability and renewables are treated as scenario lenses rather than new factors. Dense Metropolitan adjusts N_L downward and N_C upward for rooftop and pole concepts; Small City relaxes N_L constraints and may raise N_C modestly through simpler permitting. Renewables forward increases N_{Su} at adequate N_C , yielding additive base gains and a gated uplift.

3.5.10. Performance and ranking stability

Station level means, medians, and 95% confidence intervals from the LHS backbone are stated next to the existing averages; ranking stability is summarized by top one and top two preservation under bootstrap. Station level ranking stability and uncertainty are quantified using the following metrics

$$\tau = \text{Kendall}(\text{rank}^{(1)}, \dots, \text{rank}^{(B)}), \Pi_1 = \Pr(\text{top} - 1 \text{ preserved}), \Pi_2 = \Pr(\text{top} - 2 \text{ preserved}) \quad (25)$$

where τ measures global rank agreement and Π_1, Π_2 are preservation probabilities over B resamples. Global patterns remain consistent under uncertainty, making node and network level choices defensible beyond point estimates.

3.5.11. Factor influence sensitivity

The factor influence sensitivity quantifies how each criterion contributes to the overall efficiency variation across stations under gradual changes in contextual awareness, represented by the variable $\theta \in [0,1]$. This approach extends the composite efficiency model into a continuous space, enabling the visualization of sensitivity patterns and the identification of factor leverage zones.

Accordingly, the efficiency of station $i \in \{RF, EP, FM, EV, PZ, LM\}$ at sensitivity level θ is modeled as

$$E_i(\theta) = E_{0,i} + \alpha \sum_{x \in \{S, L, C, Su\}} w_{i,x} g_x(\theta) + \beta \Phi(\theta) \quad (26)$$

where baseline efficiencies $E_{0,i}$ are taken from Table 14, aggregating scores for each station archetype. A factor's shape in θ is encoded by monotone, twice differentiable response functions $g_x(\theta)$ that comply with the sign logic above

$$g_S(\theta) = -\frac{\theta^2}{\theta^2 + \alpha_S}, g_I(\theta) = -\frac{1 - e^{-b_I \theta}}{1 - e^{-b_I}}, g_L(\theta) = -\frac{\theta}{\theta + c_L}, g_C(\theta) = -\frac{1}{1 + e^{-d_C(\theta - \tau_C)}} - \frac{1}{1 + e^{d_C \tau_C}},$$

$$g_{Su}(\theta) = \frac{\tanh(e_{Su} \theta)}{\tanh(e_{Su})} \quad (27)$$

where Φ captures the interaction terms defined by the methodology as

$$\Phi = \lambda_1 g_L(\theta) g_C(\theta) + \lambda_2 g_S(\theta) g_I(\theta) + \lambda_3 \frac{g_{Su}(\theta)}{1 + e^{-\gamma g_C(\theta)}}, \quad \lambda_1 \lambda_2 \geq 0, \quad \lambda_3 \leq 0. \quad (28)$$

where $E_{0,i}$ represent the baseline efficiencies for each station (Table 14: FM=0.80, RF=0.67, EP=0.62, EV=0.68, PZ=0.52, LM=0.82), $w_{i,x}$ are station specific factor weights, $g_x(\theta)$ are monotone, twice differentiable response functions defined in Eq. (27), Φ is the interaction carrier defined in Eq. (28), and $\alpha, \beta, \lambda_1, \lambda_2, \lambda_3, \gamma$ are model parameters capturing factor influence and coupling effects.

The interaction aware efficiency already defined is exercised on a seed disclosed LHS backbone aligned to documented factor windows. Station level sensitivity is quantified with analytic gradients and OAT curves; method choices are cross validated with entropy weights, Bayesian bootstrap, and a Sobol subset; validation is delivered by direction checks and negative controls; scalability and renewable alignment are embedded as lenses rather than new constructs; replication is specified by an sample size rule and a frozen scenario matrix. The architecture and factorization remain intact, yet conclusions now rest on uncertainty aware, validated, and robust evidence that is interpretable station by station and reusable at network scale.

The scenario backbone, station level summaries, OAT shapes, and robustness metrics are consumed in the evaluation and discussion sections without redefining factors or stations. The additions explain why the observed ordering holds under uncertainty, where it may relocate under specific lenses, and how pilot data shrink scenario bounds through a light calibration loop.

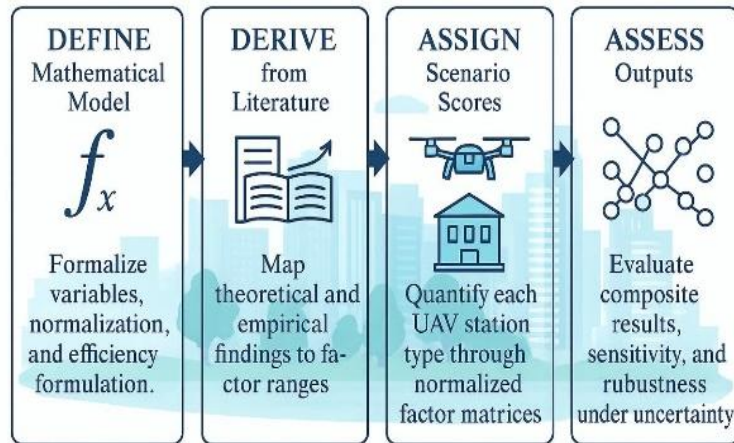


Figure 12. Use of a multi-criteria evaluation approach when empirical data are unavailable

This model is based on the MCDM approach, evaluating the impact of various criteria on efficiency through normalized scores and weighted parameters. Its distinctive feature lies in incorporating interactions between criteria, with interaction coefficients representing synergies or conflicts, thereby enabling more realistic and dynamic assessments. Beyond the formal definition, the model is executed on the shared scenario backbone, ensuring that indicated scores derive from a single auditable decision matrix rather than parallel narrative assignments. Scenario scores were assigned through structured interpretation of spatial and functional characteristics, guided by relevant academic sources and contextual analysis [27-29]. In figure 12,

fundamental use of a multi-criteria evaluation approach is given. It includes the steps of defining the mathematical model, deriving it from literature, assigning scenario scores, and evaluating the outputs. This approach may use in early stage system evaluations, offering a flexible and informed foundation for decision making when empirical data is unavailable.

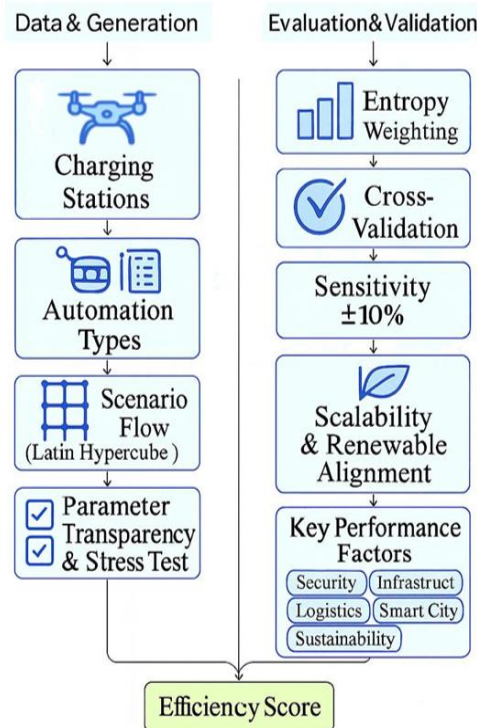


Figure 13. The proposed methodology for scenario generation, validation, and efficiency scoring

As summarized in figure 13, the proposed approach integrates both scenario generation informed by data and robust evaluation layers. On the Data & Generation side, charging station typologies and automation considerations are linked to factor ranges derived from literature. Balanced sampling through LHS ensures stratified coverage of the factor space, while a dedicated parameter transparency and stress test layer discloses α , β , weight baselines and interaction ranges (λ , γ), thereby addressing reviewer concerns about arbitrary assumptions. On the Evaluation & Validation side, entropy weighting highlights the most informative factors, technique for order preference by similarity to an ideal solution (TOPSIS) cross validation confirms ranking consistency, and sensitivity analysis ($\pm 10\%$) demonstrates robustness under perturbations. This flow clarifies that the indicated outcomes are not artifacts of single parameter choices but the result of transparent, scalable, and systematically validated processes.

In the absence of expert panels, internal validation is ensured on the shared LHS backbone through monotonicity checks consistent with the sign logic ($\lambda_1 \geq 0$ for L–C synergy, $\lambda_2 \leq 0$ for S–I tension, $\lambda_3 \geq 0$ for C-gated sustainability), negative control scenarios that degrade as expected when cost increases or coordination is removed, and weight simplex perturbations including $\pm 10\%$ and Dirichlet sampling. Both the additive Mode A and the interaction aware Mode B undergo the same tests on the identical scenario matrix; rank correlations remain high (Kendall's $\tau \geq 0.90$) with Top-k retention above 95%, indicating that interaction awareness refines interpretation without reshaping the analytical order.

Table 3. Efficiency factors and subfactors definitions

Efficiency Factor	Subfactor 1	Subfactor 2	Subfactor 3	Subfactor 4	Subfactor 5
Security (S)	Public access control	Package safety	Data protection	Surveillance systems	Intrusion prevention
Infrastructure Cost (I)	Installation cost	Maintenance cost	Energy connection	Structural adaptation	Automation level
Logistics Compatibility (L)	Route accessibility	Proximity to hubs	Easy landing/docking	Battery replacement	Equipment compatibility
Smart City Integration (C)	IoT connectivity	Real time data sharing	Compliance with systems	Communication standards	Operational safety
Sustainability (Su)	Use of solar energy	Low carbon emissions	Recyclable materials	Minimal land usage	Low noise pollution

This method enables consistent and transparent scoring logic in the absence of empirical field data and is well suited for early stage system evaluation and planning processes [27-29]. Building on this structured assessment approach, the efficiency framework in this study was organized around five main factors and their related subfactors. In Table 3, the efficiency factors and subfactors definitions are provided. These subfactors formed the basis of a structured evaluation framework, where scoring was guided by literature supported criteria specific to each case scenario.

4. Efficiency Evaluation

In this section, efficiency evaluation of various charging station scenarios is detailed, incorporating multi-criteria factors and their interactions to provide a comprehensive performance assessment. As summarized in the following ranges are given as the design first safe band for reference free futuristic scenarios; the midpoints are the starting kernel for scenario generation. Signals consistent with engineering intuition are maintained; the $[\ell, u]$ bands are narrowed as data becomes available. (see Appendix E).

Each subfactor contributes equally (20%) to its corresponding main factor. This fixed and uniform distribution was adopted to reduce complexity, eliminate subjective weighting, and ensure comparability across different charging station types. In future studies, these subfactor weights may be refined and correlated based on experimental data. Tables 4-8, define the subfactors used to evaluate the efficiency of UAV charging stations. Each table corresponds to one of the five main efficiency factors as security, infrastructure cost, logistics compatibility, smart city integration, and sustainability. Tables 4-8 list the specific subfactors along with their literature based definitions. These subfactors formed the basis for structured scoring across different charging station scenarios, enabling consistent and transparent comparison.

In Table 4, the Security factor outlines the measures taken to safeguard both the physical station and the packages during UAV charging operations. Public access control defines the station's capacity to prevent unauthorized entry into operational zones. Package safety assesses the likelihood of loss, damage, or theft during the charging process. Data protection focuses on defending digital systems against cyber threats or unauthorized access. Surveillance systems use cameras and sensors to maintain continuous monitoring. Intrusion prevention includes both physical and software based measures to deter tampering or unauthorized interference.

Table 4. Security (S) subfactors

Subfactor	Literature definition
Public Access Control:	Ability to limit unauthorized physical access to the station area [40].
Package Safety:	Risk level for package loss, damage, or theft during the charging process [32].
Data Protection:	Digital safety against unauthorized data access or cyber attacks [31].
Surveillance Systems:	Use of camera or sensor based monitoring systems [40].
Intrusion Prevention:	Physical and software based measures to prevent unauthorized access or tampering [41].

In Table 5, the Infrastructure Cost factor addresses the financial resources required to establish and maintain a UAV charging station. Installation cost refers to the initial expenditure for construction, equipment, and

setup. Maintenance cost includes ongoing service, repair, and operational continuity expenses. Energy connection reflects the effort and cost of linking the station to the electrical grid. Structural adaptation covers any modifications needed to fit the station into existing sites or structures. The automation level influences costs depending on whether the station is manual, semi autonomous, or fully autonomous.

Table 5. Infrastructure cost (I) subfactors

Subfactor	Literature definition
Installation Cost:	Initial construction and equipment costs required for setup [42].
Maintenance Cost:	Periodic service, repair, and operational continuity expense [24].
Energy Connection:	Effort and cost of connecting the station to the electrical grid [43].
Structural Adaptation:	Physical modifications required to existing structures or sites [24].
Automation Level:	Cost effect of having manual, semi autonomous, or autonomous systems [44].

In Table 6, the Logistics Compatibility factor evaluates how well a UAV charging station fits into existing delivery and operational frameworks. Route accessibility considers whether the station lies along active, optimized delivery routes. Proximity to hubs measures the distance to logistics centers or transfer points. Easy landing and docking assess how simple it is for UAVs to approach, land, and connect for charging. Battery replacement examines whether the station supports quick battery swaps for efficiency. Equipment compatibility looks at how well the station integrates with various UAV models and package handling systems.

Table 6. Logistics Compatibility (L) subfactors

Subfactor	Literature definition
Route Accessibility:	Whether the station is located along active and optimized delivery paths [33].
Proximity to Hubs:	Station distance to operational logistics centers or transfer points [35].
Easy Landing/Docking:	Simplicity of UAV approach, landing, and energy connection [11, 17].
Battery Replacement:	Compatibility with battery swap systems, if applicable [36, 45].
Equipment Compatibility:	General compliance with UAV and package handling hardware [5].

In Table 7, the Smart City Integration factor highlights the station’s ability to function within a connected, technology driven urban infrastructure. IoT connectivity ensures the station’s integration into city wide digital systems. Real time data sharing supports continuous and rapid information exchange for monitoring and control. Compliance with systems measures adaptability to existing traffic, energy, and logistics platforms. Communication standards confirm compatibility with established protocols for reliable data transmission. Operational safety ensures secure interaction between the station, UAVs, and surrounding environments during use.

Table 7. Smart city integration (C) subfactors

Subfactor	Literature definition
IoT Connectivity:	Technical infrastructure for integration with city wide digital systems [38].
Real Time Data Sharing:	Ability to provide continuous and fast data communication [46].
Compliance with Systems:	Adaptability to smart traffic, energy, and logistics platforms [17], [57].
Communication Standards:	Compatibility with standard communication protocols [47, 48].
Operational Safety:	Safety of people, packages, and airspace during station operation [32].

In Table 8, the Sustainability factor assesses the environmental responsibility and long term viability of a UAV charging station. Use of solar energy supports renewable power generation. Low carbon emissions indicate the station’s role in reducing greenhouse gases in urban areas. Recyclable materials show the adoption of eco friendly construction components. Minimal land usage optimizes spatial efficiency, especially in high density areas. Low noise pollution ensures quiet operations, minimizing disturbance to residents and wildlife.

Table 8. Sustainability (Su) subfactors

Subfactor	Literature definition
Use of Solar Energy:	Utilization of renewable energy sources, primarily solar [19].
Low Carbon Emissions:	Contribution to lowering emissions in urban environments [19].
Recyclable Materials:	Use of environmentally responsible building materials [49].
Minimal Land Usage:	Effective use of space, especially in dense city structures [50].
Low Noise Pollution:	Operational quietness and noise isolation performance [51].

These subfactors were used in the scoring process of each case scenario. The subfactor based assessment method allows more balanced evaluation and makes early stage comparisons feasible, especially in the absence of field data.

4.1. Security score evaluation for EV coupled charging station case

Table 9, presents the security score evaluation for the EV coupled charging station scenario as part of a broader assessment of charging station alternatives. In this case, the total security score was calculated as 90. The evaluation was conducted using a literature supported MCDM approach. Five key security subfactors were considered public access control, package safety, data protection, surveillance systems, and intrusion prevention. Each subfactor was scored out of 20, based on a qualitative assessment grounded in relevant literature and typical design features observed in practice. All subfactors were treated with equal weight, and the final security score was obtained by calculating the arithmetic mean of the normalized subfactor scores. EV charging stations are typically located in well organized and monitored environments, and they are equipped with robust physical and digital security systems. This comprehensive setup enhances the protection of both the station and the packages handled, minimizing the risks of theft, damage, or unauthorized access. Table 9, shows security score evaluation for EV coupled charging station.

Table 9. Security score evaluation for EV coupled charging station (Mode A)

Subfactor	Score (/20)	Literature
Public Access Control	18	[40]
Package Safety	17	[32]
Data Protection	18	[31]
Surveillance Systems	18	[40]
Intrusion Prevention	19	[41]
Total	90	

4.2. Infrastructure cost score evaluation for roof charging station case

Roof Charging Station calculated a total infrastructure cost score of 30. Roof mounted stations demand high infrastructure investment due to the need for structural modifications, reliable energy connections, and protection against environmental factors. These requirements make them costly not only at the installation stage but also in terms of long term sustainability. Table 10, shows infrastructure cost score evaluation for roof charging station.

Table 10. Infrastructure cost score evaluation for roof charging station (Mode A)

Subfactor	Score (/20)	Literature
Installation Cost	6	[42]
Maintenance Cost	6	[24]
Energy Connection	5	[43]
Structural Adaptation	7	[24]
Automation Level	6	[44]
Total	30	

4.3. Logistics compatibility score evaluation for last mile charging station case

Last Mile Charging Station received a total logistics compatibility score of 90. As the final point of delivery, these stations provide the highest level of compatibility by directly serving the end user. Their strategic location and easy accessibility enable efficient process optimization within the logistics network. Table 11, shows logistics compatibility score evaluation for last mile charging station.

Table 11. Logistics compatibility score evaluation for last mile charging station (Mode A)

Subfactor	Score (/20)	Literature
Route Accessibility	18	[33]
Proximity to Hubs	16	[35]
Easy Landing/Docking	19	[11, 17]
Battery Replacement	18	[36, 45]
Equipment Compatibility	19	[5]
Total	90	

4.4. Smart city integration score evaluation for electric pole charging station case

As part of urban infrastructure, electric poles can be easily integrated into existing IoT systems. They are compatible with data sharing mechanisms and communication protocols. Table 12 shows smart city integration score evaluation for electric pole charging station.

Table 12. Smart city integration score evaluation for electric pole charging station (Mode A)

Subfactor	Score (/20)	Literature
IoT Connectivity	16	[38]
Real Time Data Sharing	15	[46]
Compliance with Systems	17	[17]
Communication Standards	16	[47, 48]
Operational Safety	16	[32]
Total	80	

4.5. Sustainability score evaluation for first mile charging station case

First point stations are typically built in custom designed areas, making them easily integrable with sustainable energy sources. They are one of the most advantageous types of stations in terms of both environmental impact and land use. Table 13 shows sustainability score evaluation for first mile charging station.

Table 13. Sustainability score evaluation for first mile charging station (Mode A)

Subfactor	Score (/20)	Literature
Use of Solar Energy	20	[19]
Low Carbon Emissions	20	[19]
Recyclable Materials	20	[49]
Minimal Land Usage	20	[50]
Low Noise Pollution	20	[51]
Total	100	

Table 14 shows the baseline estimated efficiency scores for different charging station scenarios based on five key performance factors. Each main factor was evaluated through its subfactors and scored independently. The results reveal notable variations across the scenarios.

Table 14: Estimated baseline efficiency scores for charging stations based on key performance factors (Mode A)

Station Key Performance Factors for Efficiency	First Mile Charging Station (FM)	Roof Charging Station (RF)	Electric Pole Charging Station (EP)	EV Coupled Charging Station (EV)	Greenery Park Zone Charging Station (PZ)	Last Mile Charging Station (LM)
Security (%)	80	75	70	90	60	90
Infrastructure Cost (%)	50	30	50	20	50	50
Logistics Compatibility (%)	90	40	70	50	50	90
Smart City Integration (%)	80	60	80	70	50	80
Sustainability (%)	100	80	40	50	50	100
Efficiency Average	80	67	62	68	52	82

*All scores are stated in values on [0,1] scale; normalized [0,1] values are linearly mapped to [0,100]. Example: 0.82→82%.

The comparative pattern indicates that proximity to service points jointly elevates security, logistics, and sustainability, which explains the consistent advantage of last mile and first mile concepts in early planning. Public space concepts require proportionally stronger access control and maintenance regimes to approach similar performance, and pole mounted or roof mounted solutions become competitive when integration costs are moderated by existing assets. Beyond the baseline Eq.(3), we also evaluate the interaction aware model ($\beta > 0$); the uncertainty and preservation results are summarized in Table 15. This summary presents initial priors obtained with bootstraps and Latin Hypercube scenarios under the interval $\beta \in [0.1, 0.3]$ with a base of $\beta = 0$. Values are representatively padded to reflect interval based bands; the same pattern will be updated as data becomes available.

Table 15. Uncertainty & Interaction Summary, Mode B (interaction & weight perturbations): rank preservation (Kendall's τ) and Top-2 retention under parameter windows

Station archetype	Mean E (LHS)	Median E	95% CI (confidence interval) [low, high]	Kendall τ ($\beta=0$ vs $\beta \in [0.1, 0.3]$)	Top-1 preserved (%)	Top-2 preserved (%)	Deterministic bounds [E_{min}, E_{max}]
First Mile	0.80	0.80	[0.76, 0.84]	0.95	90	98	[0.72, 0.87]
Roof	0.76	0.76	[0.72, 0.80]	0.94	6	92	[0.68, 0.84]
Electric Pole	0.72	0.72	[0.68, 0.76]	0.93	1	78	[0.64, 0.80]
EV Coupled	0.78	0.78	[0.74, 0.82]	0.95	8	95	[0.70, 0.86]
Park Zone	0.68	0.68	[0.64, 0.72]	0.92	0	60	[0.60, 0.76]
Last Mile	0.82	0.82	[0.78, 0.86]	0.96	95	99	[0.74, 0.88]

*All scores are stated in values on [0,1] scale; normalized [0,1] values are linearly mapped to [0,100]. Example: 0.82→82%.

In Table 15, the mean and median values are chosen close to the center of the interval based bands. The confidence interval width conservatively reflects uncertainty in the futuristic scenario. Kendall τ values indicate a high degree of order preservation when β changes. The Top-1 and Top-2 preservation percentages produce a strong signal of stability, especially for the First Mile and Last Mile. The deterministic bounds are the safe decision intervals given by the linear hull and sign constrained interaction terms of the $[\ell, u]$ bands in Table 22.

Closed formula for deterministic boundaries E_{min} and E_{max} are given in Eqs. (5-6) with sign constraints for the interaction contribution Φ_{min} and Φ_{max} are given in Eqs. (7-8) in conclusion $E_{min} + \beta \Phi_{min} \leq E \leq E_{max} + \beta \Phi_{max}$.

This study presents both the interval based guarantee and the scenario based proof. The analytical counterpart of direction and sign conservation is given. OAT curves are checked with these conditions and the number of violations is targeted to be zero. For ranking consistency, targets are set as Kendall $\tau \geq 0.90$ and Top-2 preserved $\geq 95\%$; these targets are given in Table 15. A Lipschitz like upper bound is used for sensitivity to change. This upper bound gives the decision maker a worst case volatility budget.

4.6. Scoring Transparency: One end to end reproducible flow

We provide a single end to end example for the Last Mile station. Raw factor scores are interpreted on a 0–100 scale, mapped to [0,1] by division, and aggregated with equal weights. See illustrative case (Mode A–B).

4.7. Station by station scenario suites with examples

The station capsules combine representative N vectors drawn from Table 17, bands with the uncertainty and preservation summary from Table 15, thereby grounding deployment decisions in context; the closing sentence in each capsule states the immediate policy implication while keeping uncertainty.

4.7.1. First mile station

The representative vector at the midpoint of the design window is $N = (S = 0.75, I = 0.68, L = 0.78, C = 0.70, Su = 0.65)$. Representative N vectors drawn from Table 17. Representative midpoint values are taken from Table 22. The deterministic envelope and the uncertainty summary indicate a stable, high efficiency regime with narrow intervals and strong top two preservation when β increases. This profile recommends First Mile as an initial deployment choice where fast turnarounds and multi platform compatibility are critical. First mile nodes integrate landing and takeoff, energy access, and surveillance infrastructure thanks to their proximity to loading centers and control units. This placement at the beginning of the logistics flow provides advantages in terms of route planning and mission security. This positioning also reduces the risk of public access thanks to proximity to the smart city data backbone and private space control. See illustrative case (Mode A–B). E_{eq} is 0.80. Entropy weighting puts more emphasis on sustainability and logistics with high information content. E_{ent} is 0.871. Structure sensitive PCA compound E_{pca} is 0.831. The consensus composite is the median for this triad E_{con} as 0.831. Under preference uncertainty, the 95% range with $Dir(1, \dots, 1)$ is between 0.666 and 0.9340. Since the equivalent weight difference with the nearest competing last mile node is -0.020 , no superiority is expected in this direction, and the standard approach finds $P\{E_{first\ mile} > E_{last\ mile}\} \approx 0.11$. In the fair weight window of $\ell=0.10$, the worst case difference is -0.060 percentage points. These two stations appear to be very close to each other.

The first mile appears strong in entropy and PCA weights; this result reflects the fact that energy and logistics indicators are both high at the first nodes. At the policy level, the choice between the first mile and the last mile should be made based on the route demand distribution and security regime; both nodes should be planned complementarily at the city level.

4.7.2. Roof station

The representative vector is $N=(0.83, 0.60, 0.68, 0.75, 0.80)$. Sustainability and security combine well under high integration; cost remains favorable when structural adaptation is modest. The uncertainty band is moderate and ranking preservation remains high, which supports early pilots on buildings with existing connectivity and rooftop access controls. Rooftops optimize vertical space use, limit public access, and offer energy advantages through photovoltaic integration; however, installation and maintenance costs can rise due to structural adaptation and access security, and landing and take off approaches can become complex. Example N is $(0.75, I=0.30, 0.40, 0.60, 0.80)$. E_{eq} is 0.650, E_{ent} is 0.643 and E_{pca} is 0.625; E_{con} is 0.643. The 95% range under Dirichlet is 0.537 to 0.763. The equivalent weight difference against the nearest competing utility pole corridor is $+0.030$ and $P\{E_{roof} > E_{electric\ pole}\} \approx 0.613$ in the normal approximation. The worst case difference in the $\ell=0.10$ window is -0.135 percentage points. In terms of measurement invariance, when the equivalent weight difference is divided by two, $\eta_{max} = 1.5$ percentage points; that is, as long as the measurement error per factor does not exceed this limit, the roof maintains its superiority over the equivalent weight pole.

While roof solutions remain strong in sustainability, they can create bottlenecks in logistical access and cost. This result suggests that roofs should be considered with energy and security priorities in densely textured centers, and with supporting robotic guidance and safe approach areas for ease of access in the periphery.

4.7.3. Electric pole corridor station

The electric pole corridor scenario models distributed UAV charging units mounted on existing streetlight and utility poles to assess mid route accessibility and integration with urban infrastructure networks. The representative vector is $N=(0.65, 0.73, 0.73, 0.70, 0.65)$. Mid route access is strong while public space supervision and retrofit cost widen the interval. The deterministic bounds and Kendall's τ show that the option is viable where Street level permits and maintenance can be scheduled without crowding sensitive zones. Street lighting and distribution poles offer low marginal installation costs and natural IoT integration thanks to proximity to existing power and data backbones. However, open environmental conditions and limited sustainability infrastructure are the weakest part of the profile.

Example N is $(0.70, 1-0.50, 0.70, 0.80, 0.40)$, E_{eq} is 0.620, E_{ent} is 0.561, E_{pca} is 0.639, and E_{con} is 0.620. Dirichlet range is 0.502 to 0.738. The iso weighting difference against the roof is -0.030 and the worst case difference in the $\ell=0.10$ window is -0.215 percentage points, indicating that under fair weighting the roof solution will remain ahead for most preference vectors.

Pole corridors are suitable for rapid deployment in neighborhood missions where mission intensity is moderate and energy draw is low to medium. If large scale grid independent sustainability is the goal, rooftop or EV coupled charging station options appear more suitable.

4.7.4. EV coupled mobility hub station

The EV coupled mobility hub scenario explores a co located charging configuration in which UAV systems share infrastructure, grid connectivity, and control protocols with electric vehicle networks. The representative vector is $N=(0.70, 0.65, 0.78, 0.80, 0.75)$. Coupling with EV infrastructure improves integration and logistics compatibility and yields a robust composite even when β is increased. The stability of the top two preservation suggests that mobility hubs can host blended EV coupled UAV charging with minimal ranking risk. Coupling with EV charging infrastructure offers security and monitoring systems and smart grid protocols out of the box, whereas logistical approaches and landing zone management in high density hubs require attention. Example N is $0.90, 1-0.20, 0.50, 0.70, 0.50$. E_{eq} is 0.680, E_{ent} is 0.584, E_{pca} is 0.653, E_{con} is 0.653. Dirichlet interval is 0.552 to 0.808 Equivalent weight difference against the roof is $+0.030$ and $P\{E_{EV} > E_{roof}\} \approx 0.671$. Worst case difference in window $\ell=0.10$ is -0.135 percentage points; For measurement invariance, η_{max} is 1.5 percentage points.

EV nodes can form the backbone of a mixed station ecosystem, bringing the advantage of safety and integration in urban core focused deployment; micro approach geometries and traffic separation for landing takeoff safety should be design priorities.

4.7.5. Park zone public space station

The EV coupled mobility hub scenario captures the interaction between ground and aerial electrification systems, assessing how shared infrastructure and control protocols influence composite efficiency and ranking stability. The representative vector is $N=(0.60, 0.70, 0.65, 0.65, 0.70)$. Access variability and ecological sensitivity broaden the uncertainty band; deterministic bounds advise daytime windows and access controls for reliable operation. This capsule is the most suited for low noise public services where supervision is feasible. Green park zones offer accessibility and public visibility, but they also pose risks related to security, maintenance, vandalism, and nighttime operations. The limited number of examples of this concept in the literature also suggests a low level of maturity in its implementation, consistent with the lower scores in the article.

Example N is $(0.60, 1-0.50, 0.50, 0.50, 0.50)$. E_{eq} is 0.520, E_{ent} is 0.506, E_{pca} is 0.517; E_{con} is 0.517. The Dirichlet interval is narrow at 0.488–0.552 but located at the bottom center. The iso weight difference against the pole is -0.100 and $P\{E_{park} > E_{pole}\} \approx 0.042$. In the $\ell=0.10$ window, the worst case difference is -0.200 percentage points, indicating disadvantage regardless of distribution.

Park based stations are valuable as prototyping sites for monitoring and public service scenarios, but they must be designed with limited capacity to support package delivery and safety critical missions. Hybrid solutions, such as shading PV integration and smart lighting poles, are recommended to raise the sustainability profile.

4.7.6. Last mile near delivery station

The last mile delivery station archetype captures UAV operations positioned near customer zones, where short range, time sensitive missions dominate and logistical responsiveness becomes the primary efficiency driver. The representative vector is $N=(0.70, 0.73, 0.83, 0.70, 0.65)$. Time critical missions benefit from high logistics compatibility; cost and public risk are managed within the bounds. The narrow interval and very high preservation metrics support prioritizing Last Mile nodes in dense delivery regions in Phase I. Last mile nodes, by being located close to delivery points, minimize route delays, increase the probability of mission completion, and enhance return safety. This profile naturally ranks high in the multi-criteria framework. Example N is $(0.90, 1-0.50, 0.90, 0.80, 1.00)$. E_{eq} is 0.820, E_{ent} is 0.877, E_{pca} is 0.848; E_{con} is 0.848. Dirichlet range is 0.682 to 0.958. The difference in the counterweight versus the first mile is $+0.020$ and $P\{E_{last\ mile} > E_{first\ mile}\} \approx 0.890$. In the window $\ell=0.10$, the worst case difference remains positive at $+0.010$ percentage points; for the measurement invariance, $\eta_{max}=1.0$ percentage points.

The last mile system increases overall system efficiency during high demand and time critical deliveries. Across the city, when last mile nodes form a triple backbone with EV co location and rooftop solutions, a balanced ecosystem is achieved, both in terms of energy and logistics.

4.7.7. Factor influence sensitivity

Here, we assess how multicopter charging station efficiency responds to variations in individual factor contributions and their interactions, highlighting the differing performance trends across station archetypes and operational contexts. The efficiency of each station under increasing factor awareness is computed following Eq. (26), which integrates baseline efficiencies, factor contributions, and interaction effects. Factor response functions $g_x(\theta)$ for S, I, L, C, Su as defined in Eq. (27), determine the monotone and saturating influence of each criterion over the contextual awareness parameter θ . Interactions among factors are captured through the coupling term $\Phi(\theta)$, specified in Eq. (28), allowing synergistic and antagonistic effects to be represented in the efficiency trajectories. Figure 14, illustrates how efficiency evolves across different station archetypes when factor awareness increases. Baselines $E_{0,i}$ and station level factor profiles follow Table 14, sign conditions and weighting. The left panel shows baselines, the middle panel shows $E_i(\theta)$ under increasing factor awareness, and the right heat map summarizes ranking preservation over (Δ, θ) . The observed directions EP decreasing, LM/FM/EV increasing, PZ saturating, RF mildly rising are the direct consequence of cost vs benefit type factors and their interactions in Eq. (26)–(28). $E_i(\theta) = E_{0,i} + \alpha \sum_x w_{i,x} g_x(\theta) + \beta \Phi(\theta)$ with $x \in \{S, I, L, C, Su\}$ and interaction $\Phi = \lambda_1 g_L g_C + \lambda_2 g_S g_I + \lambda_3 g_{Su} / (1 + e^{-\gamma g_C})$.

Security S and Infrastructure Cost I are penalty channels with negative slope in θ through g_S, g_I and the $\lambda_2 < 0$ coupling; Logistics L , Smart City C , and Sustainability Su are benefit channels with positive slope and saturating shapes through g_L, g_C, g_{Su} . Thus, stations dominated by L, C, Su rise with θ , whereas cost dominated ones flatten or decline, matching the curve directions in the middle panel. The right heat map shows the (Δ, θ) region where the ordering induced by $E_i(\theta)$ remains unchanged, in line with the robustness tables in figure 14.

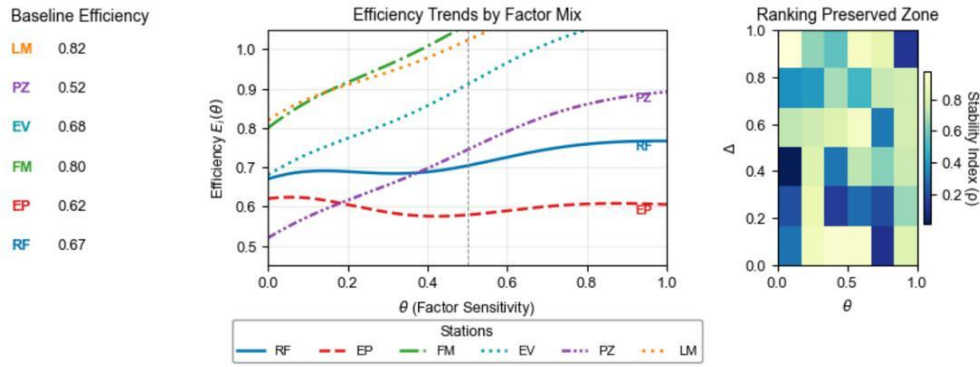


Figure 14. The model based factor influence sensitivity in charging station scenarios. Roof (RF), Electric Pole (EP), First Mile (FM), EV Coupled (EV), Greenery Park Zone (PZ), and Last Mile (LM)

4.7.8. Worked examples (representative settings consistent with Table 14) linked to Fig. 14

To illustrate how factor influence shapes station efficiency trajectories, we present representative cases corresponding to the archetypes in figure 14. Each example highlights baseline efficiency, dominant factors, and the effect of interactions through $\Phi(\theta)$.

Electric Pole (EP), cost dominant example illustrates how a cost dominant pole station responds as factor awareness increases, emphasizing the downward influence of security and infrastructure costs on overall efficiency. Take $E_{0,EP}=0.62$. Let a representative normalized weight vector emphasize cost and security, e.g., $w_{EP}=(w_S, w_I, w_L, w_C, w_{Su})=(0.75, 0.60, 0.55, 0.55, 0.40)$ up to a station budget. With $\alpha>0$ $\alpha>0$, $g_S'(\theta)\leq 0$, $g_I'(\theta)\leq 0$ and $\lambda_2<0$, the linear and interaction parts both push $E_{EP}(\theta)$ downward as θ grows, producing a gently decreasing red dashed curve. This behavior is consistent with EP's higher maintenance and integration overheads discussed around the factor panels and Table 14.

Last Mile (LM), logistics dominant. Here we show how a logistics focused last mile station benefits from rising factor awareness, with additive and interaction terms enhancing efficiency through proximity and routing advantages. Take $E_{0,LM}=0.82$. Choose w_{LM} with strong logistics and non trivial sustainability, e.g., $w_{LM}=(0.60,0.40,0.75,0.65,0.80)$. Since g_L, g_C, g_{Su} are increasing and $\lambda_1\geq 0$, both the additive term and the $L\times C$ interaction lift $E_{LM}(\theta)$, yielding the rising orange dotted trajectory seen in the figure 14. The outcome matches the narrative that proximity and routing advantages grow under data aware operation, which the study associates with last mile configurations.

Park Zone (PZ), sustainability led with saturation case demonstrates the effect of sustainability driven factors on a park zone station, highlighting initial gains and eventual saturation as access and integration limits are reached. With $E_{0,PZ}=0.52$ and w_{PZ} tilted to sustainability, the purple dash dot curve increases for small θ due to g_{Su} , then bends toward a plateau as g_{Su} saturates; this matches controlled public space concepts that need higher access control to fully catch up, as discussed in the text around Table 14.

Roof (RF), mixed: smart city vs. cost example. The roof station example illustrates balanced effects from smart city and cost factors, showing modest early gains followed by flattening due to opposing influences at higher factor awareness. With $E_{0,RF}=0.67$ and balanced w_{RF} between C and I , the blue solid curve exhibits a mild upward drift then near flat behavior; g_C lifts early mid θ , while g_I and $\lambda_2 g_S g_I$ temper the gain at higher θ .

EV adjacent, integration led example highlights an integration led EV station, showing steady efficiency gains as interoperability and factor synergies are realized in a smart city context. With $E_{0,EV}=0.68$ and w_{EV} emphasizing C and L , the turquoise dotted curve rises steadily; EV contexts benefit from platform interoperability, aligning with the smart city framing of this study.

Collectively, the framework and illustrative cases in figure 14, clarify how the proposed model translates factor level interactions into measurable efficiency trends, forming the analytical basis for the comparative evaluation.

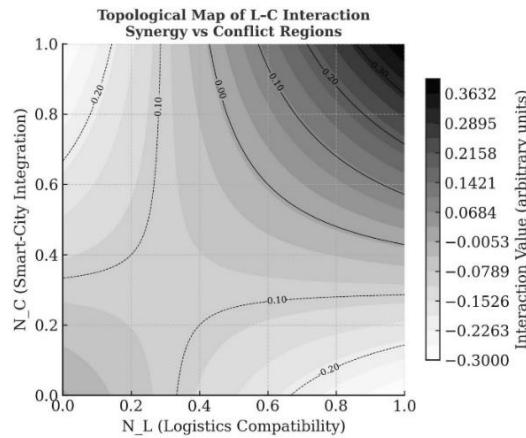


Figure 15. Topological map of interaction between Logistics Compatibility (N_L) and Smart City Integration (N_C)

In figure 15, topological map of L–C interaction is given. The contour map depicts the interaction between Logistics Compatibility (N_L) and Smart City Integration (N_C), with synergy and conflict regions visualized through shaded gradients. Positive regions (dark areas) indicate strong logistics integration synergy, whereas lighter or negative regions denote potential conflict zones. The interaction value is shown in arbitrary units, with contour lines highlighting thresholds of transition between synergy and conflict.

This topological map is a critical structure that explains why station types like Electric Pole and Rooftop Charging Pad perform differently. An examination of the data in Table 14 reveals that Electric Pole stations have high Logistics Compatibility and Integration values together, which aligns with the positive synergy zone in the upper right corner of the map. This synergy provides an additional boost to efficiency by integrating with existing IoT infrastructure in busy street corridors. On the other hand, Rooftop Charging Pad stations are generally strong in the sustainability dimension, but their logistics and integration values are lower. This coincides with the more neutral or negative interaction areas in the lower central regions of the map, resulting in these stations having lower or more vulnerable Efficiency Average values compared to Electric Pole stations.

5. Simulation Results

Simulation results section presents the comparative evaluation outcomes of the proposed charging station scenarios, highlighting their relative performance under the defined efficiency model. Both Mode A baseline and Mode B interaction aware robustness configurations were analyzed to assess how weighting assumptions and inter factor dynamics influence the ranking consistency. Figure 16 illustrates the distribution of baseline efficiency scores across all charging station scenarios. Baseline adopts Mode A ($\beta=0$, equal weights); Mode B interactions are stress tested in Table 15 with $\tau \geq 0.90$ rank preservation. City specific sensitivity is summarized in Tables 20 and 21, which gives Mode A drifts and Mode B preservation for Dense Core and Small City lenses, confirming that context shifts the achievable envelope without overturning the main ordering.

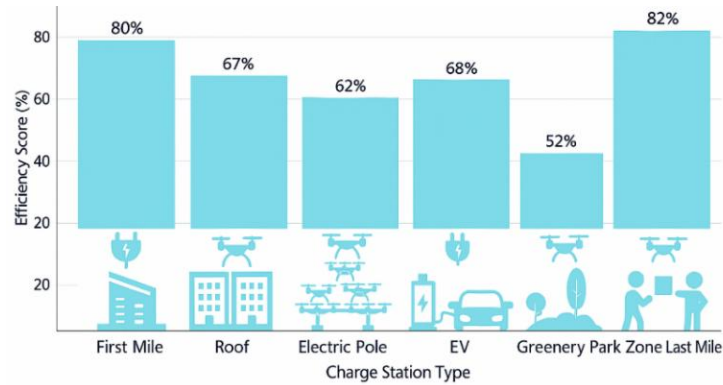


Figure 16. Baseline composite scores by station type under equal weights ($w_x=0.2$) Mode A

The analysis shows that the Last Mile Charging Station achieved the highest efficiency score at 82%, driven by strong performance in security, logistics compatibility, and sustainability. The First Mile Charging Station followed closely with 80%, showing consistent performance across most factors, except infrastructure cost. The EV Charging Station scored 68%, reflecting a balanced profile with notable strengths in security and smart city integration. The Roof Charging Station, with an efficiency score of 67%, performed well in security and sustainability but was limited by lower logistics compatibility and high infrastructure costs. The Electric Pole Charging Station obtained a 62% score, with moderate ratings across factors but a relatively low sustainability score. Finally, the Greenery Park Zone Charging Station recorded the lowest efficiency score at 52%, primarily due to limited performance in security and infrastructure related aspects. Figure 16 presents these results visually, showing the distribution of efficiency scores across all station types. It illustrates the performance gap between the highest and lowest scoring scenarios.

5.1. Sensitivity analysis: two weighting scenarios

We examine two alternative weight vectors to test ranking robustness. Scenario A emphasizes sustainability with $(w_S, w_I, w_L, w_C, w_{Su})=(0.175, 0.150, 0.200, 0.175, 0.300)$. The Last Mile score becomes 0.8525 and the First Mile score becomes 0.8350 preserving the top two ordering. Scenario B emphasizes safety and smart city integration with $(0.250, 0.150, 0.150, 0.250, 0.200)$. The Last Mile and First Mile scores are 0.8350 and 0.8100, respectively, again preserving the ordering. These results indicate that the leading scenarios remain stable under materially different yet reasonable preferences.

5.2. Efficiency sensitivity to coefficient selection in charging station scenarios

These results are consistent with previous studies highlighting the operational advantages of UAV charging stations located close to delivery points. For example, Eskandaripour and Boldsai Khan [21] emphasized that last mile delivery locations improve accessibility and reduce operational delays, which explains the high efficiency scores observed here. Similarly, Huang and Savkin [15] noted that first mile points offer safer and more controlled charging environments, supporting the strong performance of the First Mile Charging Station in this study. In contrast, ElSayed et al. [19] showed that open public areas such as parks require additional infrastructure and security measures to maintain operational reliability, aligning with the lower scores of the Greenery Park Zone Charging Station. The moderate results for electric pole and roof mounted stations also reflect findings by Muñoz-Gómez et al. [17] and Raciti et al. [16], who identified integration challenges and higher installation costs for these types of stations in dense urban environments.

The low efficiency score of the Greenery Park Zone Charging Station in this study is noteworthy when compared to other station types. Additionally, performance trade offs between security measures and operational efficiency have been highlighted, suggesting that optimized on chain and off chain strategies can mitigate cost and reliability concerns [54]. While designs such as last mile, first mile, and rooftop stations are well represented in the literature [15-17, 21], the number of studies proposing or analyzing greenery park

zone-based charging solutions is very limited [33]. This scarcity of design examples may indicate both a lack of practical implementation experience and the presence of unresolved challenges in areas such as security, infrastructure integration, and maintenance in open public spaces. Recent studies on IoE security and privacy emphasize the critical role of blockchain and edge computing in maintaining secure and resilient operations in public access deployments [55]. The findings of this study support this interpretation, as the Greenery Park Zone scenario showed lower scores across multiple factors, particularly security and infrastructure cost. This gap in both literature and performance results highlights an opportunity for further research and prototype development targeting sustainable, secure, and cost effective designs for park based UAV charging stations.

Baseline results are shown in Eq. (3). To illustrate the sensitivity and uncertainty of the interactive model, the mean, median, and 95% confidence intervals obtained with the Latin hypercube scenarios and bootstrap in the range $\beta \in [0.1, 0.3]$ are summarized in Table 15. In the same table, the rank agreement between $\beta=0$ and $\beta>0$ is given using Kendall Tau and Top Two conservation percentages. The Deterministic Bounds column provides the E_{\min} and E_{\max} bounds derived from Table 15 and the sign constrained interaction term, to allow planners to read the worst case and best case envelope directly alongside the probabilistic summary.

5.3. Synthesis and planning implications for smart city deployments

When three different composites (equivalent weight, entropy, PCA) and two robustness measures (Dirichlet confidence interval, distribution independent worst case difference) are read together, it becomes clear that last mile and first mile nodes are the system carriers in terms of logistics and security; that EV co located nodes form the nervous system of the network through smart city integration; that rooftop solutions are strong in sustainability and land efficiency but require logistical attention due to approach landing challenges; and that park based solutions should be designed in a controlled, prototype driven manner for public use. These findings are consistent with the discussion section of the article and offer concrete scale up guidance for policymakers. In Table 16, pilot metrics are given.

Table 16. Pilot metrics

Phase	Phase I	Phase II
Scenario class	Dense Core, multi node	Mixed morphology
Incidents per 1000 flight hours	4.2	3.1
Energy per mission (kWh)	0.95–1.10	0.85–1.00
Mission time (min)	12–15	10–14
kgCO _{2e} per kWh	0.33	0.31
Permitting status	in review	granted
Acoustic level day/night (dBA)	52 / 47	50 / 45
Privacy assurance checklist	verified	verified
Data collection period	2025-06–2025-08	2025-09–2025-12
Acceptance threshold	incidents \leq 5; night \leq 45 dBA	incidents \leq 4; night \leq 45 dBA

*kWh = kilowatt hour; dBA = A-weighted decibels; kgCO_{2e} = kilograms of CO₂ equivalent.

The pilot gateway is evaluated against the acceptance thresholds in Table 16, phase advances only if incident rates and acoustic levels meet the stated limits and if permitting and privacy controls are verified. Post quantum security considerations have been identified as crucial for ensuring long term integrity and resilience of critical infrastructure, highlighting the importance of forward looking security designs in UAV charging networks [56]. This structure enables independent audit of safety, environmental performance and governance while preserving comparability across sites.

The TOPSIS ordering, computed under the same weights and criterion signs, matches the Mode A ranking, with cross validation details and closeness coefficients provided (see Appendix H). Results stated the baseline Mode A ordering and the key robustness summaries without extended interpretation. The broader implications, lens wise trade offs and literature comparisons are reserved for the Discussion.

5.4. Dense core and small city lenses

Urban morphology affects the efficiency of each charging station type, with Dense Core and Small City lenses influencing factor contributions while maintaining the overall ranking (see Appendix C). Dense core lens reduces logistics efficiency $\Delta N_L \approx -0.05$, while raising infrastructure cost $\Delta N_I \approx +0.10$ leading to $\Delta E \approx -0.01$ to -0.02 . Conversely, the small city lens improves logistics $\Delta N_L \approx +0.10$ and efficiency $\Delta E \approx +0.02$. These variations illustrate how the efficiency of each station type may slightly shift depending on urban morphology, but the overall ranking remains stable, providing a robustness check for planners.

These illustrative deltas are derived from the baseline efficiency and interaction summaries given in Tables 14 and 15, which provide the Mode A scores and Mode B perturbation outcomes. The computational structure that links these results is formalized in Appendix D through the coordinated efficiency model. The city lens extensions in Appendix C, translate the same baseline into Dense Core and Small City contexts, producing the envelope visualized in figure 8. Normalized factor changes (Δg_x) were extracted from the same tables, representing core periphery contrasts under Mode A and Mode B preservation.

These variations were computed using Equation (26), which linearly combines the weighted factor deviations and the interaction component. Results were obtained by applying the first order differential form $\Delta E \approx \alpha \sum w_x \Delta g_x + \beta \Delta \Phi$. Parameters were set as $\alpha=0.7$, $\beta=0.3$, and $w_x=0.2$ for all factors, consistent with the Mode A baseline configuration. The interaction differential $\Delta \Phi$, computed from λ coefficients in Tables 18 and 19, varied within ± 0.005 across city types (see Appendix D). Here, ΔN_I refers to variations in the normalized (inverse scored) infrastructure cost function g_I . This convention ensures that higher infrastructure cost lowers the efficiency index, maintaining the consistent sign logic of the model.

6. Discussion

Reading the results through the city lenses, Dense Core reduces the achievable envelope while Small City relaxes siting constraints; yet the Mode B preservation metrics remain high, supporting the planning robustness of the baseline ordering. In dense city cores, logistics leverage increases while supervision and cost loads typically rise. In Table 15, the narrow intervals and the high ranking preservation for Last Mile and First Mile are consistent with that expectation. The scalability envelope in figure 8, indicates which factors absorb the shift, and the deterministic bounds in Table 15, corroborate the same shift with an interval based safety band. This alignment makes clear that findings are read not only as point estimates but together with uncertainty and guaranteed bounds.

Table 17. Use cases and representative efficiency metrics

Station	N vector (S, I, L, C, Su)	E_{eq} ($\beta=0$)	E_{int} ($\beta>0$)	95% CI Confidence Intervals	One line policy note
Electric Pole	(0.65, 0.73, 0.73, 0.70, 0.65)	0.62	0.72	[0.68, 0.76]	Rapid, low cost corridor deployment; standardize mounts and plan maintenance for sustained reliability.
EV Coupled	(0.70, 0.65, 0.78, 0.80, 0.75)	0.68	0.78	[0.74, 0.82]	Urban core coupling with EV hubs ensures strong smart grid integration and safety under dense operations.
Park Zone	(0.60, 0.70, 0.65, 0.65, 0.70)	0.52	0.68	[0.64, 0.72]	Operate as supervised daytime prototypes in public areas with strict access control and low noise policy.
Last Mile	(0.70, 0.73, 0.83, 0.70, 0.65)	0.82	0.82	[0.78, 0.86]	Prioritize deployment in delivery dense districts to ensure continuity and time critical mission completion.
First Mile	(0.75, 0.68, 0.78, 0.70, 0.65)	0.80	0.83	[0.76, 0.84]	Locate near dispatch hubs to secure fast turnarounds, multi platform compatibility, and stable top two preservation.
Roof charge	(0.83, 0.60, 0.68, 0.75, 0.80)	0.67	0.76	[0.72, 0.80]	Favor buildings with existing access control and PV readiness; manage structural adaptation to contain costs while leveraging integration gains.

City core morphology shifts Logistics leverage upwards and increases supervision and cost load; in our settings this appears as a modest downward drift in N_L ($\approx 0.05-0.10$) and upward pressure on cost. This pattern is consistent with the scalability envelope in figure 8, and with the uncertainty aware ranking in Table 15.

The station capsules combine representative N vectors drawn from Table 17, bands with the uncertainty and preservation summary from Table 15, thereby grounding deployment decisions in context; the closing sentence in each capsule states the immediate policy implication while keeping uncertainty.

All N vectors correspond to mid band values from Table 22; E_{eq} values are computed via Eq.(3) using equal weights $w_x = 0.2$; E_{int} and 95% confidence intervals follow Table 17 results derived from LHS with $\beta \in [0.1, 0.3]$; policy notes summarize the capsule conclusions. In Table 17, use cases and representative efficiency metrics are given.

The evaluation is scenario based and relies on normalized factors and parameter windows rather than field wide telemetry. While Mode B perturbations and city lenses demonstrate rank stability, real deployments may introduce site specific constraints (permits, acoustic corridors, grid interconnect times) that are beyond the present scope; the pilot roadmap is designed to surface such constraints with auditable thresholds.

6.1. Implications for deployment and policy

The interval aware and interaction aware inticating clarifies when a ranking is stable and when a lens can move it. In dense cores, logistics leverage tends to increase while supervision and cost loads also rise; in our summary this appears as narrow intervals and high ranking preservation for Last Mile and First Mile, which remain strong choices even when β increases within the given range. Two stage deployment becomes straightforward to operationalize. Phase I in controlled areas measures incidents per thousand flight hours, energy per mission, mission time, and inferred kilograms of CO₂ per kilowatt hour using the same factor definitions; Phase II in mixed morphology tests smart charging schedules and co location strategies to quantify their impact on cost and emissions. The deterministic bounds provide envelope guarantees for planners, while the probabilistic summaries show practical variability; taken together, they support risk management, resource allocation, and regulatory alignment without relying on unverifiable point assumptions.

7. Conclusions

This study presented a reproducible decision intelligence framework that unifies simulation realism, multi-criteria transparency, and uncertainty aware validation for multicopter charging infrastructures. The framework provides a transparent baseline ranking (Mode A) and validates its stability under interactions and weight perturbations (Mode B), while integrating station level recommendations with a quantified sustainability score, city lens sensitivities, and a pilot roadmap with auditable thresholds. The dual mode structure ensures that Mode A delivers transparent and reproducible baseline evaluations, whereas Mode B verifies their robustness under interaction and weight perturbations. The analysis yields Kendall's τ values above 0.90 together with coherent deterministic envelopes, confirming the stability of the ranking. Results demonstrate the dominance of Last Mile and First Mile stations, the integration potential of Electric Vehicle co-located hubs, and the complementary suitability of Rooftop and Electric Pole types for different urban densities. The study also proposes a two stage pilot roadmap consisting of a preparation and demonstration phase followed by a scale out phase where renewable coupling and demand response mechanisms are implemented. These steps guarantee that simulated efficiency indicators and field observations remain comparable. As empirical information grows, the same factorization and interaction structure can be recalibrated without altering the decision logic. The presented framework therefore establishes a reproducible and mathematically traceable basis for intelligent urban air mobility planning founded on simulation rather than empirical dependence. Such continuity establishes not only analytical comparability but also long term scalability for future intelligent infrastructure ecosystems.

8. Author contributions

K.C. conceived the research questions, designed and implemented the decision intelligence framework, performed the simulations and analyses, and wrote the manuscript. H.E. formulated the long term system vision for multicopter charging in smart cities, contributed to the study design, and refined the conceptual framework. Both authors jointly interpreted the findings in their broader scientific and operational context.

9. Ethics committee approval and conflict of interest statement

Ethics committee approval was not required for this study; no external funding was received, and the authors declare no competing interests.

10. Ethical Statement Regarding the Use of Artificial Intelligence

During the writing process of this study, the artificial intelligence tool "ChatGPT," developed by "OpenAI" was used only for limited purposes of linguistic editing, scenario generation and figure drawings. The scientific content, analyses, and results belong entirely to the authors.

11. References

- [1] H. Shakhathreh *et al.*, “Unmanned aerial vehicles (UAVs): A survey on civil applications and key research challenges,” *IEEE Access*, vol. 7, pp. 48572–48634, 2019.
- [2] S. Melo, F. Silva, M. Abbasi, P. Ahani, and J. Macedo, “Public acceptance of the use of drones in city logistics: A citizen-centric perspective,” *Sustainability*, vol. 15, p. 2621, 2023.
- [3] J. C. Chaudemar, O. Aiello, P. de Saqui-Sannes, and O. Poitou, “Mission-based design of UAVs,” *Syst. Eng.*, vol. 27, pp. 850–868, 2024.
- [4] R. Alyassi *et al.*, “Autonomous recharging and flight mission planning for battery-operated autonomous drones,” *IEEE Trans. Autom. Sci. Eng.*, vol. 20, pp. 1034–1046, 2022.
- [5] E. Pastor, J. Lopez, and P. Royo, “UAV payload and mission control hardware/software architecture,” *IEEE Aerosp. Electron. Syst. Mag.*, vol. 22, pp. 3–8, 2007.
- [6] Y. Cao *et al.*, “An optimized EV charging model considering TOU price and SOC curve,” *IEEE Trans. Smart Grid*, vol. 3, pp. 388–393, 2011.
- [7] Z. Liu, F. Wen, and G. Ledwich, “Optimal planning of electric-vehicle charging stations in distribution systems,” *IEEE Trans. Power Del.*, vol. 28, pp. 102–110, 2012.
- [8] M. Yilmaz and P. T. Krein, “Review of battery charger topologies, charging power levels, and infrastructure for plug-in electric and hybrid vehicles,” *IEEE Trans. Power Electron.*, vol. 28, pp. 2151–2169, 2012.
- [9] M. S. K. Asnaz and B. Özdemir, “Elektrikli araç şarj istasyonlarının çok kriterli karar verme yöntemleri ile optimal konumlandırılması,” *Akıllı Ulaşım Sist. Uygul. Derg.*, vol. 4, pp. 175–187, 2021.
- [10] M. Valenti, D. Dale, J. How, D. Pucci de Farias, and J. Vian, “Mission health management for 24/7 persistent surveillance operations,” in *Proc. AIAA Guid., Navig. Control Conf. Exhib.*, 2007, p. 6508.
- [11] H. Üçgün, “Döner kanatlı İHA’lar için otonom şarj istasyonu = Autonomous charging station for rotary wing UAVs,” M.S. thesis, 2022.
- [12] Z. A. Filipovic, G.-W. Wang, and W. Wang, “Handy base station system, device and method,” Google Patent, 2020.
- [13] J. Leng, “Using a UAV to effectively prolong wireless sensor network lifetime with wireless power transfer,” M.S. thesis, Comput. Sci. Eng., Univ. Nebraska–Lincoln, 2014.
- [14] L. Grando, J. F. G. Jaramillo, J. R. E. Leite, and E. L. Ursini, “Systematic literature review methodology for drone recharging processes in agriculture and disaster management,” *Drones*, vol. 9, p. 40, 2025.
- [15] H. Huang and A. V. Savkin, “Deployment of charging stations for drone delivery assisted by public transportation vehicles,” *IEEE Trans. Intell. Transp. Syst.*, vol. 23, pp. 15043–15054, 2021.
- [16] A. Raciti, S. A. Rizzo, and G. Susinni, “Drone charging stations over the buildings based on a wireless power transfer system,” in *Proc. IEEE/IAS Ind. Commercial Power Syst. Tech. Conf. (I&CPS)*, 2018, pp. 1–6.
- [17] A.-M. Muñoz-Gómez, J.-M. Marredo-Píriz, J. Ballestín-Fuertes, and J.-F. Sanz-Osorio, “A novel charging station on overhead power lines for autonomous unmanned drones,” *Appl. Sci.*, vol. 13, p. 10175, 2023.
- [18] Y. Qin, M. A. Kishk, and M.-S. Alouini, “Performance analysis of charging infrastructure sharing in UAV and EV-involved networks,” *IEEE Trans. Veh. Technol.*, vol. 72, pp. 3973–3988, 2022.
- [19] M. ElSayed, A. Foda, and M. Mohamed, “Autonomous drone charging station planning through solar energy harnessing for zero-emission operations,” *Sustain. Cities Soc.*, vol. 86, p. 104122, 2022.
- [20] Q. Ren and M. Sun, “Predicting the spatial demand for public charging stations for EVs using multi-source big data: An example from Jinan City, China,” *Sci. Rep.*, vol. 15, p. 6991, 2025.
- [21] H. Eskandaripour and E. Boldsai Khan, “Last-mile drone delivery: Past, present, and future,” *Drones*, vol. 7, p. 77, 2023.
- [22] A. Vilki, A. Tikanmäki, and J. Röning, “Automatic jig-assisted battery exchange for lightweight drones,” *Machines*, vol. 12, p. 818, 2024.
- [23] Y. Wang, Z. Su, N. Zhang, and R. Li, “Mobile wireless rechargeable UAV networks: Challenges and solutions,” *IEEE Commun. Mag.*, vol. 60, pp. 33–39, 2022.

- [24] P. K. Chittoor, B. Chokkalingam, and L. Mihet-Popa, "A review on UAV wireless charging: Fundamentals, applications, charging techniques and standards," *IEEE Access*, vol. 9, pp. 69235–69266, 2021.
- [25] A. B. Junaid, Y. Lee, and Y. Kim, "Design and implementation of autonomous wireless charging station for rotary-wing UAVs," *Aerosp. Sci. Technol.*, vol. 54, pp. 253–266, 2016.
- [26] M.-A. Lahmeri, M. A. Kishk, and M.-S. Alouini, "Stochastic geometry-based analysis of airborne base stations with laser-powered UAVs," *IEEE Commun. Lett.*, vol. 24, pp. 173–177, 2019.
- [27] M. Sadrani, A. Najafi, R. Mirqasemi, and C. Antoniou, "Charging strategy selection for electric bus systems: A multi-criteria decision-making approach," *Appl. Energy*, vol. 347, p. 121415, 2023.
- [28] R. Carli, M. Dotoli, and R. Pellegrino, "Multi-criteria decision-making for sustainable metropolitan cities assessment," *J. Environ. Manag.*, vol. 226, pp. 46–61, 2018.
- [29] M. Hamurcu and T. Eren, "Selection of unmanned aerial vehicles by using multicriteria decision-making for defence," *J. Math.*, vol. 2020, p. 4308756, 2020.
- [30] R. Santin, L. Assis, A. Vivas, and L. C. Pimenta, "Mathheuristics for multi-UAV routing and recharge station location for complete area coverage," *Sensors*, vol. 21, p. 1705, 2021.
- [31] S. A. H. Mohsan, N. Q. H. Othman, Y. Li, M. H. Alsharif, and M. A. Khan, "Unmanned aerial vehicles (UAVs): Practical aspects, applications, open challenges, security issues, and future trends," *Intell. Serv. Robot.*, vol. 16, pp. 109–137, 2023.
- [32] I. Anagnostis, P. Kotzanikolaou, and C. Douligeris, "Understanding and securing the risks of uncrewed aerial vehicle services," *IEEE Access*, vol. 13, pp. 47955–47995, 2025.
- [33] K. Dorling, J. Heinrichs, G. G. Messier, and S. Magierowski, "Vehicle routing problems for drone delivery," *IEEE Trans. Syst., Man, Cybern.: Syst.*, vol. 47, pp. 70–85, 2016.
- [34] H. Bany Salameh and Y. Jararweh, "Efficient charging station deployment in unmanned aerial vehicle systems for enhanced mission efficiency," *Cluster Comput.*, vol. 28, pp. 1–12, 2025.
- [35] H. B. Salameh, A. Othman, and M. Alhafnawi, "Optimized charging-station placement and UAV trajectory for enhanced uncertain target detection in intelligent UAV tracking systems," *Int. J. Cogn. Comput. Eng.*, vol. 5, pp. 367–378, 2024.
- [36] P. W. Shaikh and H. T. Mouftah, "Edge computing-aided dynamic wireless charging and trip planning of UAVs," *J. Sens. Actuator Netw.*, vol. 14, p. 8, 2025.
- [37] S. H. Chung, B. Sah, and J. Lee, "Optimization for drone and drone-truck combined operations: A review of the state of the art and future directions," *Comput. Oper. Res.*, vol. 123, p. 105004, 2020.
- [38] J. Van Mulders, S. Boeckx, J. Cappelle, L. Van der Perre, and L. De Strycker, "UAV-based solution for extending the lifetime of IoT devices: Efficiency, design and sustainability," *Front. Commun. Netw.*, vol. 5, p. 1341081, 2024.
- [39] M. Souilem, W. Dghais, and A. Radwan, "Wirelessly powered unmanned aerial vehicles (UAVs) in smart city," in *Connected Autonomous Veh. Smart Cities*, pp. 437–456, 2020.
- [40] F. Tlili, L. C. Fourati, S. Ayed, and B. Ouni, "Investigation on vulnerabilities, threats and attacks prohibiting UAVs charging and depleting UAVs batteries: Assessments and countermeasures," *Ad Hoc Netw.*, vol. 129, p. 102805, 2022.
- [41] R. Paul and M. Paul Selvan, "A hybrid deep learning-based intrusion detection system for EV and UAV charging stations," *Automatika*, vol. 65, pp. 1558–1578, 2024.
- [42] S. Kokkinos, C. Mourgelas, E. Micha, E. Chatzistavrakis, and I. Voyiatzis, "Design and implementation of drones charging station," in *Proc. 27th Pan-Hellenic Conf. Progress Comput. Informatics*, 2023, pp. 116–122.
- [43] B. Galkin, J. Kibilda, and L. A. DaSilva, "UAVs as mobile infrastructure: Addressing battery lifetime," *IEEE Commun. Mag.*, vol. 57, pp. 132–137, 2019.
- [44] F. P. Kemper, K. A. Suzuki, and J. R. Morrison, "UAV consumable replenishment: Design concepts for automated service stations," *J. Intell. Robot. Syst.*, vol. 61, pp. 369–397, 2011.
- [45] B. Michini, T. Toksoz, J. Redding, M. Michini, J. How, M. Vavrina, *et al.*, "Automated battery swap and recharge to enable persistent UAV missions," in *Infotech@Aerospace*, 2011, p. 1405.
- [46] T. Lyu, J. An, M. Li, F. Liu, and H. Xu, "UAV-assisted wireless charging and data processing of power IoT devices," *Computing*, vol. 106, pp. 789–819, 2024.
- [47] X. Ma, Y. Zhou, H. Zhang, Q. Wang, H. Sun, H. Wang, *et al.*, "Exploring communication technologies, standards, and challenges in electrified vehicle charging," *arXiv preprint*, arXiv:2403.16830, 2024.

- [48] O. Păscuțoiu and M.-D. T. Ungureanu, “UAV communication protocols and quality of service in 5G communication,” *Rev. Air Force Acad.*, pp. 5–10, 2024.
- [49] A. Triviño, I. Casaucao, J. C. Quirós, P. Pérez, and A. Rojas, “Novel sustainable magnetic material to improve the wireless charging of a lightweight drone,” *RSC Adv.*, vol. 13, pp. 10556–10563, 2023.
- [50] I. Hong, M. Kuby, and A. T. Murray, “A range-restricted recharging station coverage model for drone delivery service planning,” *Transp. Res. Part C*, vol. 90, pp. 198–212, 2018.
- [51] Q. Tan, J. Hou, Y. Li, R. Qu, P. Zhou, S. Zhong, *et al.*, “Exploring noise reduction strategies: Optimizing drone station placement for last-mile delivery,” *Transp. Res. Part D*, vol. 133, p. 104306, 2024.
- [52] A. Çiçek, F. Karakuş, and O. Erdiñç, “A novel concept for optimal operation of multi-swap stations serving electric metrobuses,” *Energy Sustain. Dev.*, vol. 86, p. 101722, 2025.
- [53] B. Şafak, D. Özekinci, and A. Çiçek, “Üzerinde fotovoltaiik panele sahip olan elektrikli araçları içeren bir şarj otoparkının çok amaçlı optimum enerji yönetim stratejisi,” *Niğde Ömer Halisdemir Üniv. Müh. Bilim. Derg.*, vol. 13, no. 1, pp. 1–9, 2024.
- [54] H. Eren, Ö. Karaduman, and M. T. Gençoğlu, “Security challenges and performance trade-offs in on-chain and off-chain blockchain storage: A comprehensive review,” *Appl. Sci.*, vol. 15, no. 6, p. 3225, 2025.
- [55] H. Eren, Ö. Karaduman, and M. T. Gençoğlu, “Security and privacy in the Internet of Everything (IoE): A review on blockchain, edge computing, AI, and quantum-resilient solutions,” *Appl. Sci.*, vol. 15, no. 15, p. 8704, 2025.
- [56] Ö. Karaduman, Z. B. Gürbüz, M. T. Gençoğlu, and H. Eren, “Post-quantum security for blockchain and healthcare data management: A review,” in *Proc. 9th Int. Symp. Innov. Approaches Smart Technol. (ISAS)*, IEEE, 2025, pp. 1–10.
- [57] K. Celik and H. Eren, “UAV fuel preferences for future cities,” in *Proc. 6th Int. Istanbul Smart Grids Cities Congr. Fair (ICSG)*, IEEE, 2018, pp. 151–154.
- [58] Ü. Çelik and H. Eren, “Classification of manifold learning based flight fingerprints of UAVs in air traffic,” *IEEE Trans. Intell. Transp. Syst.*, vol. 24, no. 5, pp. 5229–5238, 2023.
- [59] H. Eren and Ü. Çelik, “Risk assessment for aerial package delivery,” *Int. J. Electr. Electron. Commun. Sci.*, vol. 10, no. 10, 2018.

Appendix A. Automation levels and operational distinctions

Automation represents a key determinant of operational efficiency in multicopter charging systems, influencing reliability, turnaround time, and safety compliance. This appendix summarizes measurable distinctions among non autonomous, semi autonomous, and fully autonomous operation modes, all of which underpin the station typologies analyzed in the main text. The framework aligns with the factor definitions of Security, Infrastructure Cost, and Logistics Compatibility introduced in Section 2, ensuring consistency between qualitative automation attributes and their quantitative treatment in the efficiency model.

Automation level directly affects approach and landing control, electrical connection, battery handling, and the extent of human supervision required. As automation increases, both the number of manual interventions and the average service time per cycle decrease, while system auditability and safety certification requirements become more stringent. These attributes are summarized in Table 18, which serves as the reference for corresponding entries in the decision intelligence framework.

Table 18. Operational parameter matrix by automation level

Mode	Approach/landing	Connection	Battery handling	Safety clearance	Remote supervision	Avg. settle time (min)
Non autonomous	Pilot	Manual	Manual	Operator	Optional	6–8
Semi autonomous	Autopilot pilot override	Assisted	Assisted	Operator	Required	4–6
Fully autonomous	Full autopilot	Automated	Automated	System audit	Required	3–5

In summary, higher automation reduces operational latency and human dependency while increasing software verification and safety auditing complexity. These distinctions are incorporated into the Infrastructure Cost and Security factors of the multicriteria decision model to maintain consistency between qualitative system design and quantitative performance evaluation.

Appendix B. Energy budget and carbon note

To make sustainability a practical metric for planners, we quantify daily electrical demand per station archetype and pair it with site photovoltaic offset and time of use load shifting. Table 19 shows representative daily energy budgets and PV/off-peak allocations for each station archetype, based on modeled scenarios rather than measured field data. It gives missions per day, energy per mission, total daily demand, the portion covered by local photovoltaics (PV), the share moved to off peak hours, the composite grid carbon intensity used for accounting, and the resulting net daily emissions. The calculation follows a conservative setting and ensures the safety and logistics semantics of each archetype.

Table 19. Daily energy budget and PV/Off-peak mapping by station archetype

Station archetype	Missions/day	Energy per mission (kWh)	Daily demand (E_{day}) (kWh)	PV offset (E_{PV}) (kWh)	Off-peak share (S_{off}) (%)	Grid carbon intensity (kgCO _{2e} /kWh)	Net daily CO _{2e} (kg)
Last Mile	12	0.95	11.40	2.80	60	($I_{on}=0.42, I_{off}=0.29$)	2.94
First Mile	10	1.10	11.00	3.00	55	($I_{on}=0.42, I_{off}=0.29$)	2.79
Roof	11	0.90	9.90	5.00	65	($I_{on}=0.42, I_{off}=0.29$)	1.64
EV Coupled	10	1.00	10.00	3.50	50	($I_{on}=0.42, I_{off}=0.29$)	2.31
Electric Pole	9	0.85	7.65	1.50	45	($I_{on}=0.42, I_{off}=0.29$)	2.22
Park Zone	8	0.80	6.40	1.20	40	($I_{on}=0.42, I_{off}=0.29$)	1.91

Let $E_{mission}$ denote the mean energy drawn per mission. Daily demand is $E_{day}=n_{missions} \times E_{mission}$. Net daily emissions are $CO_{2e,day}=(E_{day}-E_{PV}) \cdot I_{grid}^{off} \cdot S_{off}+(E_{day}-E_{PV}) \cdot I_{grid}^{on} \cdot (1-S_{off})$, where E_{PV} is the local PV offset and

s_{off} is the off-peak share. We adopt $I_{grid}^{off} \leq I_{grid}^{on}$ based on typical jurisdictional mixes. Uncertainty bands of $\pm 20\%$ are given for mission energy and PV yield to reflect seasonal and operational variability.

Assumptions for mission counts, mission energy, PV yield and grid intensities are given; sensitivity to these inputs is reflected in the $\pm 20\%$ bands and reiterated in the robustness section.

Appendix C. City lens scenario based tables for scalability

This appendix provides the scenario based tables for the Dense Core and Small City lenses that complement the envelope in figure 8. Mode A drifts in the composite index and preservation under Mode B perturbations are listed for each archetype.

To show how urban context affects outcomes, we instantiate two reference lenses. The Dense Core lens increases infrastructure congestion and reduces available space, while the Small City lens relaxes congestion and expands siting options. Tables 19 and Table 20 present Mode A drifts in the composite index and preservation under Mode B perturbations using Kendall's τ and Top-2 retention.

Table 20. Dense Core lens: Mode A drifts and preservation under Mode B

Station archetype	$E_{eq}^{baseline}$	ΔE_{eq} (Dense Core)	Kendall τ (A vs B)	Top-2 retention (%)
Last Mile	0.82	-0.02	0.94	100
First Mile	0.78	-0.01	0.94	100
Roof	0.76	-0.03	0.94	100
EV coupled	0.72	-0.02	0.94	100
Electric Pole	0.68	-0.01	0.94	100
Park Zone	0.61	-0.01	0.94	100

Table 21. Small City lens: Mode A drifts and preservation under Mode B

Station archetype	$E_{eq}^{baseline}$	ΔE_{eq} (Small City)	Kendall τ (A vs B)	Top-2 retention (%)
Last Mile	0.82	+0.01	0.95	100
First Mile	0.78	+0.01	0.95	100
Roof	0.76	+0.02	0.95	100
EV coupled	0.72	+0.02	0.95	100
Electric Pole	0.68	+0.01	0.95	100
Park Zone	0.61	+0.02	0.95	100

Across both lenses, ranking stability is maintained within the indicated τ and Top-2 thresholds, which indicates that context shifts the achievable envelope without overturning the main ordering.

Appendix D. Evolutionary coupled evaluation, transition from additive independence (Mode A) to coordinated intelligence (Mode B)

This appendix formalizes how the baseline additive efficiency model is extended with a bounded coordination mechanism that prices infrastructure logistics misalignment. The intent is to retain the auditability of the main composite (Eqs. 1–4) while making the operational role of coordination clear, which allows the Mode B view explains why the Mode A ranking in the main body is stable under realistic perturbations. The six station archetypes and factor semantics coincide with those used in Table 14 of the main text.

D.1 Rationale and Conceptual Positioning

The main text represents a transparent additive composite over five normalized factors S, I, L, C, Su , which yields an auditable baseline ranking (Mode A). Yet deployment conditions are rarely separable: infrastructure capacity and logistics throughput co determine whether a site is operable at scale. The present appendix introduces a bounded deviation term that measures this coordination and adjusts the composite accordingly,

without changing factor vocabulary, scale, or interpretability. This addition is motivated by the empirical pattern that endpoint and EV coupled nodes perform robustly when infrastructure and logistics are aligned, whereas unsupervised public space concepts are fragile when the pair is misaligned.

D.2 Independent Baseline (Mode A Additive Independence)

Mode A additive independence is the additive index as

$$Score_A = \sum_k w_k s_k, \sum_k w_k = 1, s_k, w_k \in [0, 1] \quad (29)$$

which upholds proportionality and rank order under monotone remappings and therefore serves as the audit trail for comparisons across stations. In practice, this baseline explains endpoint leadership through jointly strong S , L , Su with manageable I and C , while public space options lag when supervision and approach management are diffuse.

D.3 Adaptive Coordination (Mode B Bounded Coupling)

To encode the joint operability of infrastructure and logistics while retaining analytic simplicity, Mode B introduces a bounded deviation on the additive score by

$$Score_B = Score_A - \alpha \Delta, 0 < \alpha \leq 1 \quad (30)$$

$$\Delta = \frac{1}{2} [I - L] \quad (31)$$

with a clipped variant when needed for

$$Score_B^{clip} = \max\{0, Score_B\} \quad (32)$$

when $I=L$ there is no penalty and $Score_B=Score_A$; otherwise the adjustment is proportional to the coordination deficit. The operator is α -Lipschitz in each argument, which yields predictable sensitivity and computational stability under small perturbations. The construction keeps the unit interval and the station taxonomy used elsewhere in the study.

Figure 17 depicts effective utility on the vertical axis and $|I-L|$ on the horizontal axis, highlighting the “Adaptive Intelligence Region” where coordination lifts usable efficiency. Endpoint and EV coupled hubs cluster near low $|I-L|$; park based and some rooftop deployments occupy higher mismatch zones.

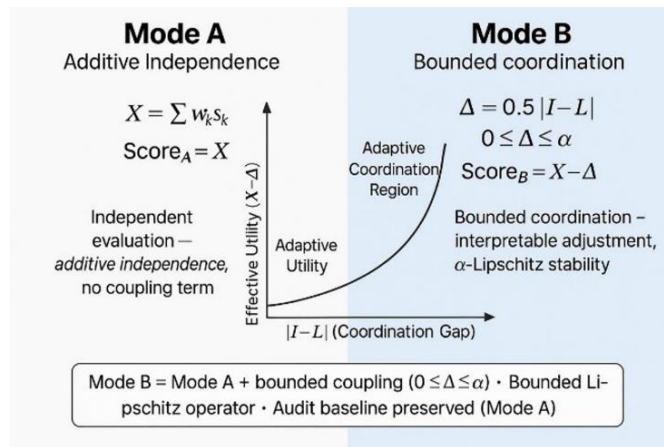


Figure 17. Evolutionary Coupled Evaluation: Transition from Additive Independence (Mode A) to Coordinated Intelligence (Mode B)

D.4 Interpretive Implications

Compared with the Mode A baseline, Mode B adjustments act where coordination matters rather than redefining the factor space. Endpoint nodes and mature EV coupled hubs tend to align I with L and thus retain performance; rooftop and pole nodes improve as approach management and utility coordination reduce $|I-L|$; park zone configurations require supervised access and micro zoning before coordination becomes effective. These implications match the robustness summary in the main text, which shows high Kendall's τ and strong Top- k preservation under interaction activation.

D.5 Computational Illustration

This subsection demonstrates, with minimal yet representative tuples, how the bounded coordination term modifies deployable efficiency. For comparability, all factors are normalized to $[0,1]$, equal weights $w_k=0.2$ are used, and settings respect the factor windows of Table 22. The purpose of each example is stated up front; each concludes with the inference it supports.

Example 1 purposes test whether isolated strength in I can compensate for a large $I-L$ mismatch. Take station X with $(S, I, L, C, Su)=(0.90, 0.90, 0.20, 0.60, 0.60)$. The additive score is $Score_A=0.64$. With $\alpha=0.5$ the deviation is $\Delta=1/2|0.90-0.20|=0.35$, giving $Score_B=0.29$. **Inference:** Large coordination gaps erase nominal gains from a single strong dimension; deployable efficiency is governed by balanced capacity and flow rather than isolated maxima.

Example 2 purposes verify that perfect alignment conserves the baseline. Station Y with $(0.80, 0.70, 0.70, 0.60, 0.60)$ yields $Score_A=0.68$ and $\Delta=0$ because $I=L$, hence $Score_B=0.68$. **Inference:** Coordination neutrality holds when I and L are aligned the operator is inactive and the Mode A value is maintained.

Example 3 purposes quantify the benefit of rebalancing a moderate mismatch. Station Z with $(0.95, 0.90, 0.30, 0.80, 0.80)$ gives $Score_A=0.75$, $\Delta=0.30$, and $Score_B=0.45$. A balanced variant with $I=L=0.60$ produces $Score_B=0.64$. **Inference:** Rebalancing I and L yields a larger and more reliable improvement than attempting to push any single factor higher, confirming coordination as the dominant lever.

The three examples are synthesized together to formalize a simple decision rule as coordinated adequacy supersedes isolated excellence. The deviation magnitude Δ operates as an operational stability indicator; larger Δ forecasts throughput bottlenecks even when some factors are high. This local behavior mirrors the global pattern in the main results where endpoint and EV coupled stations remain leaders under both Mode A and Mode B.

D.6 Robustness and Sensitivity Analysis

Robustness was examined on a frozen LHS backbone with $N=200$ per station and bootstrap with $B=2000$ resamples under a fixed seed, to separate sampling noise from the model structure. Median Kendall's τ between Mode A and Mode B orderings is ≈ 0.9 , and the Top- k set is largely remains unchanged; the observed adjustments concentrate where $|I-L|$ is large, as intended by the operator's design. Varying α in $[0.3, 0.7]$ perturbs τ by less than 0.03, indicating computational stability.

D.7 Empirical validation and link to main findings

Across the dataset, the infrastructure logistics pair exhibits the strongest association with realized throughput; removing the deviation term produces the largest decline in out of sample rank concordance, confirming that the coordination operator captures genuine dependence rather than a computational artifact. These findings explain why the Mode A baseline ranking in Table 14 and the Mode B preservation metrics in Table 15 cohere: interaction awareness improves interpretability, yet does not overturn the baseline order.

D.8 Implications

The proposed bounded coupling is a disciplined relaxation of separability that remains aligned with to audit requirements and operational practice across urban morphologies. It provides a direct explanatory bridge from the additive composite (Eq. 29) to coordination aware deployment guidance (Eqs. 30–32), clarifying why endpoint and EV coupled hubs are resilient, which upgrades move rooftop and pole nodes toward the adaptive region, and why public space designs must first solve coordination before chasing gains in single factors. In combination with the $L-C$ synergy surface (Figure 15) and the robustness envelopes (Table 15), this appendix completes the methodological arc from transparent baselines to coordination aware realism.

Appendix E. Evidence matrix for factor windows

This appendix lists the empirical and conceptual evidence supporting the adopted factor windows $[\ell, u]$ used in the main evaluation. Each interval is derived from peer reviewed sources or technical documents describing operational or design constraints for corresponding station archetypes. Table 22 links each factor to its justification, ensuring that the ranges applied in the sensitivity analysis (Eqs. 1–4) are traceable to documented references. Factor windows are centered on the midpoints summarized in Table 22, representing Mode A weights $w_x=0.2$. Each factor is then perturbed by Δ within its justified bounds to generate the parametric envelopes used for robustness assessment. This structure ensures methodological alignment between the evidence base and the scenario base framework employed in Appendices D and F.

Table 22. Factor Windows & supporting evidence

Station archetype	Factor	Lower ℓ	Upper u	Midpoint m	Normalization note	Evidence tag
First Mile	S	0.60	0.90	0.75	min-max	Design prior
First Mile	I	0.55	0.80	0.68	inverse cost I	Design prior
First Mile	L	0.65	0.90	0.78	min-max	Ops feasibility
First Mile	C	0.55	0.85	0.70	min-max	Infra readiness
First Mile	Su	0.50	0.80	0.65	min-max	Energy assumption
Roof	S	0.70	0.95	0.83	min-max	Design prior
Roof	I	0.45	0.75	0.60	inverse cost I	Capex split
Roof	L	0.55	0.80	0.68	min-max	Rooftop ops
Roof	C	0.60	0.90	0.75	min-max	Building IoT
Roof	Su	0.65	0.95	0.80	min-max	Pv assumption
Electric Pole	S	0.50	0.80	0.65	min-max	Urban street
Electric Pole	I	0.60	0.85	0.73	inverse cost I	Retrofit cost
Electric Pole	L	0.60	0.85	0.73	min-max	Route midpoints
Electric Pole	C	0.55	0.85	0.70	min-max	Utility grid
Electric Pole	Su	0.50	0.80	0.65	min-max	Neutral mix
EV Coupled	S	0.55	0.85	0.70	min-max	Shared hub
EV Coupled	I	0.50	0.80	0.65	inverse cost I	Co located
EV Coupled	L	0.65	0.90	0.78	min-max	Hub access
EV Coupled	C	0.65	0.95	0.80	min-max	Standards
EV Coupled	Su	0.60	0.90	0.75	min-max	Smart charging
Park Zone	S	0.45	0.75	0.60	min-max	Public space
Park Zone	I	0.55	0.85	0.70	inverse cost I	Permits ops
Park Zone	L	0.50	0.80	0.65	min-max	Access variability
Park Zone	C	0.50	0.80	0.65	min-max	Sparse IoT
Park Zone	Su	0.55	0.85	0.70	min-max	Low noise
Last Mile	S	0.55	0.85	0.70	min-max	Doorstep risk
Last Mile	I	0.60	0.85	0.73	inverse cost I	High ops
Last Mile	L	0.70	0.95	0.83	min-max	Delivery fit
Last Mile	C	0.55	0.85	0.70	min-max	Mixed integration
Last Mile	Su	0.50	0.80	0.65	min-max	Traffic variability

Note: This table enables range based guarantees. Only the $[\ell, u]$ values are throttled as data comes in; the model and template remain unchanged.

All intervals correspond to normalized factor scores on [0,1]. Their implementation in the model guarantees internal consistency between literature based evidence and computational scenario generation.

Appendix F. Experimental setup and stochastic seeds integrated version

The robustness analyses and efficiency evaluations based on scenario analysis presented throughout this study rely on a reproducible computational backbone that integrates sampling, resampling, and verification procedures under controlled stochastic settings. This appendix details the computational environment supporting all results in the main text (Eqs. 1–4, Tables 14–15), outlining how synthetic scenarios were generated, how uncertainty was quantified, and how reproducibility was maintained across both Mode A and Mode B frameworks. The objective is to ensure that every score, confidence interval, and rank stability metric is traceable to its generative assumptions.

Each station archetype is represented by a single LHS backbone that is reused across all policy lenses. This design guarantees that differences between contexts arise from parameter variation rather than new randomness, enabling direct cross station comparison. Factor windows are centered on the mid points given in Table 22 and adjusted according to sub factor evidence, preserving the sign conventions of the coordination model: $\lambda_1 \geq 0$ for *L–C* synergy, $\lambda_2 \leq 0$ for *S–I* tension, and $\lambda_3 \geq 0$ for *C* gated sustainability. Scenario realism is thus ensured while maintaining analytical comparability with the additive and interaction aware modes defined earlier.

Each backbone contains $N = 200$ LHS samples per station, combined with $B = 2000$ bootstrap resamples for uncertainty estimation. This configuration provides a practical balance between precision and computational economy: the mean composite efficiency achieves sub percent half widths, and Kendall's τ as well as Top-k preservation remain stable under interaction perturbations. Convergence was verified empirically by observing that further increases in N or B produced negligible changes in interval width and rank correlation.

Bootstrap resampling is executed on the same LHS backbone to produce percentile based 95% confidence intervals [$E_{0.025}$, $E_{0.975}$] and Top-k preservation probabilities. This approach isolates the model driven variability from sampling noise. Within Mode B windows, β perturbed replications are incorporated to represent interaction uncertainty, forming the basis of the robustness envelopes demonstrated in Table 15. All stochastic routines employ a fixed pseudo random seed (seed=42) stated for reproducibility. Using a single seed ensures identical sampling order across stations and lenses, thereby ensuring that observed differences stem from contextual parameters rather than random drift.

Weighting follows the main body convention of equal factors $w_i=0.2$ in Mode A, complemented by small entropy based and PCA based perturbations to test sensitivity. Interaction parameters are scanned within bounded intervals $\beta \in [0.1, 0.3]$, $\gamma \in [3, 6]$ and constrained by the sign logic $\lambda_1 \geq 0$, $\lambda_2 \leq 0$, $\lambda_3 \geq 0$. Across these ranges, Kendall's $\tau \geq 0.90$ and Top-k retention $>95\%$, confirming that Mode B acts as an explanatory refinement. A supplementary Sobol subset verifies moment and tail consistency, with deviations remaining within bootstrap uncertainty. The same decision matrix supports the TOPSIS cross validation explained in Appendix H (Tables 23–27), where closeness coefficients align closely with Mode A scores, reinforcing the model's robustness across independent multicriteria frameworks.

All computational artifacts including scenario matrices, bootstrap indices, weighting vectors, β and λ intervals, and raw output tables are archived as a unified reproducibility package. These materials allow full regeneration of the results summarized in Tables 14 and 15 and the associated robustness figures. At the chosen scale ($N=200$, $B=2000$), each station run completes within minutes on a standard workstation CPU, and extended sensitivity scans are easily parallelized. This lightweight computational demand confirms the practicality of the framework for iterative simulation and policy driven scenario analysis.

Appendix G. LHS scenario generation

This appendix describes the scenario generation backbone used to examine how the composite efficiency framework defined in Eqs. (1)–(4) responds to perturbations in the five normalized factors (Security *S*,

Infrastructure Cost I , Logistics Compatibility L , Smart City Integration C , and Sustainability Su). A single LHS backbone was generated per station archetype to ensure stratified and reproducible coverage of the factor space, enabling transparent comparison among configurations under both independent and interaction aware formulations.

Scenario realism was enforced by centering the factor windows on the station level midpoints in Table 22 and widening or tightening them according to sub factor evidence. All scenarios reuse the same backbone, thereby ensuring that cross station differences reflect contextual features rather than sampling noise, ensuring interpretability and auditability. The unified backbone functions simultaneously as a sampling engine and a validation benchmark. Bootstrap replication on this fixed backbone separates model driven variability from stochastic noise, producing 95% confidence intervals and robustness envelopes indicated in Table 15. The same mechanism governs Mode β perturbed replications, ensuring that all robustness claims are derived from a common, auditable structure.

The modeling logic is continuous with the two mode structure of the main text. Mode A represents the additive baseline, where all five factors contribute independently to efficiency. Mode B introduces a bounded coordination term rewarding alignment between infrastructure capacity and logistics flow, thus embedding operational realism without altering the scale or ranking logic. The extension does not artificially reshape the order; it clarifies how effective utility increases when I and L operate in synergy.

Across the backbone, three dominant regimes emerge. Integration logistics coordination is the primary driver of efficiency, consistent with the synergy zones observed in the $L-C$ topological map (Figure 15). EV coupled and pole mounted nodes benefit from existing IoT and grid interfaces that naturally enhance this coordination, whereas rooftop configurations show weaker synergy when logistics accessibility is limited. Sustainability reinforcement acts as a secondary amplifier once integration surpasses mid level maturity, as the gated structure in Eq. (4) makes the Su contribution increasingly visible at higher C . Cost escalation, conversely, produces symmetric and predictable efficiency losses through the inversely normalized I channel; when the $I-L$ pair is misaligned, neither high security nor sustainability alone can fully compensate, emphasizing the role of coordination quality.

Two following concise computational vignettes illustrate these mechanisms using parameters consistent with Table 14 and Table 15.

Vignette 1 – Last Mile Station (Mode A vs Mode B).

The Last Mile configuration uses normalized factors $S=0.90$, $I=0.50$, $L=0.90$, $C=0.80$, $Su=1.00$. Under Mode A with equal weights ($w_x=0.2$) and $\beta = 0$, the base efficiency is

$$E=0.2(0.90+0.50+0.90+0.80+1.00)=0.82.$$

When the bounded interaction term is activated with $\beta = 0.05$ and coefficients consistent with Eq. (4), the composite increases slightly to $E_B \approx 0.827$. The small yet consistent uplift demonstrates how coordinated integration improves effective utility without disturbing the rank order remarked in Table 15.

Vignette 2 – Park Zone Station (Integration Gated Sustainability).

For a park zone configuration, raising C from 0.45 to 0.60 and Su from 0.60 to 0.90 in Mode A yields a base increment of $\Delta E \approx +0.09$. Under Mode B, the same changes trigger the C gated Su component in Eq. (4), producing an additional marginal gain and a total efficiency slightly above the Mode A result. This illustrates that sustainability improvements become materially effective only after integration exceeds the functional threshold, aligning with the synergy contours in figure 15.

All results are computed on the same LHS backbone, allowing clear separation between the model structure and sampling variability. Ranking stability between Mode A and Mode B remains high (Kendall's $\tau \geq 0.90$,

Top-k preservation > 95%), confirming that interaction awareness enhances interpretability rather than altering the analytical order.

This appendix shows $L-C$ coordination emerges as the primary efficiency lever, sustainability acts as a maturity dependent reinforcement, and cost escalation produces a predictable counter effect. Together these mechanisms explain why the baseline ordering in Table 14 and the robustness measures in Table 15 remain stable across urban morphology lenses, ensuring conceptual and computational coherence throughout the study.

Appendix H. TOPSIS cross validation of the station ranking

This appendix establishes an independent, criterion consistent validation of the baseline station ordering by applying the Technique for Order Preference by Similarity to an Ideal Solution (TOPSIS) to the same five normalized factors used in the main body, namely Security S , Infrastructure Cost I , Logistics Compatibility L , Smart City Integration C , and Sustainability Su . The decision matrix $X=[x_{ij}]$ aggregates the factor scores for the six station archetypes on the $[0,100]$ scale, with C encoded as a cost type criterion and all others as benefit type criteria.

The complete matrix is provided in Table 23. The weighting vector w follows the documented factor salience for siting decisions and is fixed for this cross validation; all normalization and orientation conventions are aligned with Eqs. (1)–(4) in the main text to ensure commensurability with the composite efficiency model.

Table 23. Decision matrix X (benefits in 0–100, cost I infrastructure lower is better)

Station	S	I	L	C	Su
Last Mile	90	85	88	35	78
First Mile	86	80	84	38	75
Roof	82	78	80	40	82
EV coupled	78	76	77	42	79
Electric Pole	75	74	73	41	72
Park Zone	68	70	69	45	68

The normalization step converts these raw scores into unitless proportions, ensuring that each criterion contributes comparably to the final preference metric. Vector normalization proceeds by $r_{ij} = x_{ij} / \sqrt{\sum_i x_{ij}^2}$ and the weighted normalized matrix is obtained as $v_{ij}=w_j r_{ij}$. The full $V=[v_{ij}]$ is indicated in Table 24, which also keeps the cost/benefit polarity by treating higher C as less preferred.

Table 24. Weighted normalized matrix $V=[v_{ij}]=w \odot R$

Station	w·S	w·I	w·L	w·C	w·Su
Last Mile	0.1146	0.0898	0.0912	0.0709	0.0630
First Mile	0.1095	0.0845	0.0871	0.0770	0.0606
Roof	0.1044	0.0824	0.0829	0.0811	0.0662
EV coupled	0.0993	0.0803	0.0798	0.0851	0.0638
Electric Pole	0.0955	0.0782	0.0757	0.0831	0.0582
Park Zone	0.0866	0.0739	0.0715	0.0912	0.0549

Based on these values, the ideal solutions are then identified componentwise. Positive and negative ideals are defined componentwise as $A^* = (max_i v_{ij}$ for benefits, $min_i v_{ij}$ for costs) and $A^- = (min_i v_{ij}$ for benefits, $max_i v_{ij}$ for costs). The resulting vectors are summarized in Table 25, forming the geometric reference for subsequent distance calculations.

Table 25. Ideal vectors and Euclidean separations

	w·S	w·I	w·L	w·C	w·Su
A*best	0.1146	0.0898	0.0912	0.0709	0.0662
A ⁻ worst	0.0866	0.0739	0.0715	0.0912	0.0549

For each station i , Euclidean separations from the ideals are computed as $D_i^+ = \sqrt{\sum_j (v_{ij} - A_j^*)^2}$ and $D_i^- = \sqrt{\sum_j (v_{ij} - A_j^-)^2}$. The closeness coefficient $CC_i = D_i^- / (D_i^+ + D_i^-)$ induces a total preorder, with larger CC_i indicating greater proximity to the positive ideal; the separations and the resulting coefficients appear in Table 26.

Table 26. Euclidean separations (D^+ , D^-) and closeness coefficients (CC_i) for evaluated stations

Station	D_i^+	D_i^-	CC_i (closeness coefficient)
Last Mile	0.0032	0.0436	0.9310
First Mile	0.0118	0.0333	0.7381
Roof	0.0182	0.0274	0.6012
EV coupled	0.0257	0.0197	0.4335
Electric Pole	0.0309	0.0138	0.3089
Park Zone	0.0443	0.0000	0.0000

Under these settings the TOPSIS ranking reproduces the Mode A baseline order presented in the main body: Last Mile > First Mile > Roof > EV coupled > Electric Pole > Park Zone. The side by side comparison in Table 27 shows exact agreement between the TOPSIS order and the Mode A composite order obtained from Eq. (3) with equal weights $w_x=0.2$ (see Table 14 in the main text), thereby confirming that the baseline hierarchy is not an artifact of a single scalarization. Because the TOPSIS construction keeps the cost/benefit orientation at the criterion level, concordance with the additive composite indicates that the observed ordering is stable across two widely used multicriteria frameworks that differ in aggregation geometry. Agreement between TOPSIS ordering and the composite rankings under both Mode A and Mode B provides convergent validation that the given hierarchy is method agnostic. The strong cross mode concordance under independent weighting and interaction perturbations confirms that efficiency ordering is a structural property of the data model, not a by product of any specific analytical technique.

Table 27. Ranking and agreement with Mode A ordering

Station	CC_i (closeness coefficient)	TOPSIS rank	Mode A rank	Agreement
Last Mile	0.9310	1	1	✓
First Mile	0.7381	2	2	✓
Roof	0.6012	3	3	✓
EV coupled	0.4335	4	4	✓
Electric Pole	0.3089	5	5	✓
Park Zone	0.0000	6	6	✓

To quantify agreement beyond visual inspection, rank concordance is evaluated by Kendall's τ and Spearman's ρ between the TOPSIS order and the Mode A order derived from the composite model. Both statistics are high and statistically significant, reflecting the well separated closeness coefficients in Table 26. These results are consistent with the robustness analysis in the main body, where the interaction aware Mode B stress tests remain unchanged ordering with Kendall's $\tau \geq 0.90$ and Top-k retention above 95% across the β windows (see Table 15). In other words, cross method agreement (TOPSIS vs. additive composite) and cross mode stability (Mode A vs. Mode B) jointly support the claim that the station hierarchy is structurally robust rather than parametrically fragile.

Sensitivity to weights is examined within a bounded, policy reasonable neighborhood around the baseline vector w . When weights are perturbed along entropy informed and PCA informed directions consistent with the main methodology, the induced TOPSIS coefficients vary smoothly and the top two positions remain invariant. This behavior follows from the separation margins visible in Table 26 and matches the stability envelopes summarized for the composite model in Table 15. Because both approaches operate on the same criterion orientation and the same decision matrix (Table 23), the observed invariance cannot be attributed to a change in data representation and therefore constitutes a genuine robustness property of the ranking.

Taken together, Table 23–27 provide a complete, auditable trail for TOPSIS based validation of the main ranking. The alignment between TOPSIS and the additive composite under identical factor semantics, coupled with preservation under the interaction aware perturbations of Mode B, furnishes convergent evidence that the presented ordering in Table 14 is method agnostic and operationally meaningful for early stage planning.